JCI insight

WNK1 regulates uterine homeostasis and its ability to support pregnancy

Ru-pin Alicia Chi, Tianyuan Wang, Chou-Long Huang, San-Pin Wu, Steven Young, John Lydon, Francesco DeMayo

JCI Insight. 2020. https://doi.org/10.1172/jci.insight.141832.

Research In-Press Preview **Reproductive biology**

WNK1 is an atypical kinase protein ubiquitously expressed in humans and mice. A mutation in its encoding gene causes hypertension in humans which is associated with abnormal ion homeostasis. WNK1 is critical for in vitro decidualization in human endometrial stromal cells, thereby demonstrating its importance in female reproduction. Using a mouse model, WNK1 was ablated in the female reproductive tract to define its in vivo role in uterine biology. Loss of WNK1 altered uterine morphology, causing endometrial epithelial hyperplasia, adenomyotic features and a delay in embryo implantation, ultimately resulting in compromised fertility. Combining transcriptomic, proteomic and interactomic analyses revealed a novel regulatory pathway whereby WNK1 represses AKT phosphorylation through the phosphatase PP2A in endometrial cells from both humans and mice. We show that WNK1 interacts with PPP2R1A, the alpha isoform of the PP2A scaffold subunit. This maintains the levels of PP2A subunits and stabilizes its activity, which then dephosphorylates AKT. Therefore, loss of WNK1 reduced PP2A activity, causing AKT hypersignaling. Using FOXO1 as a readout of AKT activity, we demonstrate that there was escalated FOXO1 phosphorylation and nuclear exclusion, leading to a disruption in the expression of genes that are crucial for embryo implantation.

WNK1 regulates uterine homeostasis and its ability to support pregnancy

Ru-pin Alicia Chi[1], Tianyuan Wang[2], Chou-Long Huang[3], San-pin Wu[1], Steven Young[4], John Lydon[5], and Francesco DeMayo[1]

[1] Reproductive and Developmental Biology Laboratory, National Institute of Environmental Health Sciences, Durham, NC, 27709, USA
[2] Integrative Bioinformatics Support Group, National Institute of Environmental Health Sciences, Durham, NC, 27709, USA
[3] Department of Internal Medicine, University of Iowa Carver College of Medicine, Iowa, IA, 52242, USA
[4] Department of Obstetrics and Gynecology, University of North Carolina at Chapel Hill, Chapel Hill, NC, 27599, USA
[5] Department of Molecular and Cellular Biology, Baylor College of Medicine, Houston, TX, 77030, USA

Conflict of interest statement:

The authors have declared that no conflict of interest exists.

Correspondence to:
Francesco DeMayo
National Institute of Environmental Health Sciences
111 T.W. Alexander Drive
P.O. Box 12233, Mail Drop B2-3
Research Triangle Park, NC 27709
Ph: (984)-287-3987
Email: francesco.demayo@nih.gov

Keywords:

WNK1, reproduction, implantation, AKT, PP2A, FOXO1, adenomyosis, hyperplasia

Abstract

WNK1 is an atypical kinase protein ubiquitously expressed in humans and mice. A mutation in its encoding gene causes hypertension in humans which is associated with abnormal ion homeostasis. WNK1 is critical for *in vitro* decidualization in human endometrial stromal cells, thereby demonstrating its importance in female reproduction. Using a mouse model, WNK1 was ablated in the female reproductive tract to define its *in vivo* role in uterine biology. Loss of WNK1 altered uterine morphology, causing endometrial epithelial hyperplasia, adenomyotic features and a delay in embryo implantation, ultimately resulting in compromised fertility. Combining transcriptomic, proteomic and interactomic analyses revealed a novel regulatory pathway whereby WNK1 represses AKT phosphorylation through the phosphatase PP2A in endometrial cells from both humans and mice. We show that WNK1 interacts with PPP2R1A, the alpha isoform of the PP2A scaffold subunit. This maintains the levels of PP2A subunits and stabilizes its activity, which then dephosphorylates AKT. Therefore, loss of WNK1 reduced PP2A activity, causing AKT hypersignaling. Using FOXO1 as a readout of AKT activity, we demonstrate that there was escalated FOXO1 phosphorylation and nuclear exclusion, leading to a disruption in the expression of genes that are crucial for embryo implantation.

INTRODUCTION

Aberrant embryo implantation results in a ripple effect leading to pregnancy complications and miscarriages (1). Embryo implantation occurs during the “window of receptivity” and requires a fully prepared and responsive uterus. WNK1, (with no lysine (k) kinase 1) have been identified as a potential regulator of uterine function acting downstream of EGFR which regulates endometrial stroma cell proliferation, migration and differentiation *in vitro* (2, 3). These findings indicate a previously unrecognized function of WNK1 in the female reproductive tract and led us to hypothesize that WNK1 is a mediator of uterine function.

WNK1 belongs to a family of serine/threonine protein kinases (4, 5), with its name derived from the unusual placement of the catalytic lysine in subdomain I (6). To date, WNK1’s function is the most extensively explored in the kidney and the nervous system due to the link between its mutation and familial hypertension and autonomic neuropathy (7-9). In the renal system, WNK1 controls ion homeostasis through diverse mechanisms including activation of the SGK1/epithelial sodium channel pathway (10), regulating the potassium channel Kir1.1 cell surface localization (11), as well as controlling the activity of Na-K-Cl cotransporter through phosphorylating OSR1(OXSR1) and SPAK (12, 13). Interestingly, WNK1’s regulatory function on OSR1 is critical for cardiovascular development, thereby contributing to embryonic lethality when ablated from the endothelium (14, 15). These findings suggest that although WNK1 exhibits organ-specific physiological functions, the underlying cellular components regulated by WNK1 may share similarity between the different tissues.

Despite its ubiquitous expression, WNK1's role in organs other than those described above remain unexplored. Given the role of WNK1 in regulating uterine stromal cell biology *in vitro*, we hypothesized that WNK1 is essential in regulating uterine functions. To test this, we genetically ablated *Wnk1* in the mouse female reproductive tract and demonstrate that WNK1 is critical in maintaining uterine morphology, regulating epithelial proliferation and permitting appropriate embryo implantation. Transcriptomic and proteomic analyses identified deregulation of the AKT signaling pathway underlying the observed phenotypes. Using cultured human endometrial cells, we conducted a series of functional analyses to tease out the mechanisms of WNK1's function in uterine biology.

RESULTS

WNK1 is expressed in the uterus during the window of implantation in both humans and mice

WNK1 expression was examined by IHC in human endometrium during the proliferative and mid-secretory phases as well as in the peri-implantation uterus of mice. In humans, WNK1 is expressed in both the epithelium and stroma during the proliferative and mid-secretory phases (Fig. 1.A). Similarly in mice, WNK1 is expressed during and after implantation on gestation days (GDs) 4.5 and 5.5 (Fig. 1.B). These findings support the *in vivo* involvement of WNK1 in regulating functions of the female reproductive tract.

WNK1 ablation altered uterine morphology and microenvironment

To examine WNK1's function in the female reproductive tract, we crossed the conditional *Wnk1* allele mice ($Wnk1^{f/f}$) to the PGR^{Cre} mice (14, 16), and confirmed that in the $PGR^{Cre/+}$;$Wnk1^{f/f}$ offspring ($Wnk1^{d/d}$), CRE mediated excision led to the removal of exon 2 (Fig. S1.A and S1.B). The whole-uterus WNK1 level was confirmed to be reduced in the $Wnk1^{d/d}$ uteri (Fig. S1.C), which decreased by 7.1-fold according to densitometrical quantification of the signal intensity. The WNK1 expression detected in the $Wnk1^{d/d}$ mice were due to immune and endothelial cells which do not express PGR.

A tissue clearing technique was employed to visualize uterine morphology in 3D during the window of receptivity (Fig. 2.A) (17). WNK1 deficiency caused an increased number and altered structure of the endometrial glands (Fig. 2.A). Among the abnormalities observed in the $Wnk1^{d/d}$

uteri was the failure of gland reorientation surrounding the embryo (18). This is seen in the *Wnk1*$^{f/f}$ uteri where glands near the embryo exhibited a elongated structure while glands away from the embryo remained tortuous and intertwined. In the *Wnk1*$^{d/d}$ uteri, the glands appears equally tortuous irrespective of distance from embryo (Fig. 2.A). Examination of uterine cross sections from older mice (26 and 50 weeks) further demonstrated invasion of glands into the myometrium, suggesting that WNK1 ablation caused adenomyosis-like features (Fig. 2.B). This was supported by the elevated expression of *Moesin* (*Msn*) in the *Wnk1*$^{d/d}$ uteri, a biomarker for adenomyosis in humans (Fig. 2.C) (19). Quantification of gland number and *Foxa2* gene expression showed significant elevation in the *Wnk1*$^{d/d}$ uteri (Fig. 2.D and E), confirming the substantial increase in glandular tissues. To examine whether the increased glands was a result of increased proliferation in the uterus, we examined two mitotic markers - cyclin D1 (CCND1) and phosphorylated histone H3 (H3S10p). Elevated levels of both proteins in the glandular epithelium of the *Wnk1*$^{d/d}$ uteri were observed (Fig. 2.F). In addition, higher expression of both proteins was also observed in the luminal epithelium of *Wnk1*$^{d/d}$ uteri demonstrating that WNK1 ablation induced epithelial hyperplasia was not restricted to the glands, but also apparent in the luminal epithelium. Moreover, we observed increased extracellular matrix deposition especially surrounding the glands in the *Wnk1*$^{d/d}$ uteri, as shown by Masson's trichrome staining (Fig. 2.G). These results suggest that the adenomyotic phenotype could be associated with increased epithelial proliferation as well as excessive extracellular matrix deposition (20, 21).

Uterine loss of WNK1 compromised fertility and impaired implantation

A breeding trial was conducted to determine the impact of WNK1 ablation on female fertility. Here, both the *Wnk1*$^{f/f}$ and *Wnk1*$^{d/d}$ female mice were mated one-on-one to wildtype males for 6 months, during which the mice were closely monitored for pregnancy and delivery (Table S1). Of the 13 control mice, 11 were able to complete the breeding trial (85%), with 2 found dead midtrial.

Necropsy showed neither pregnancy nor abnormality associated with the reproductive tract in these two mice, indicating that the cause of death was not related to abnormal uterine function. The 11 mice produced 52 litters totaling 355 pups, which was equivalent to 5 litters and 6.8 pups per litter during the 6 months (Fig. 3.A). In contrast, only 9 of the 14 *Wnk1*$^{d/d}$ mice initiated in the trial were able to complete the trial (64%), owing to 5 females succumbing to complications during pregnancy or delivery. Of those, 2 were found dead near term each carrying 2 pups, 2 were in dystocia and had to undergo euthanization. One was found ill and necropsy showed utero-abdominal fistula. Of the 9 females that completed the trial, 14 litters and 37 pups were produced, which averaged to 1.6 litters and 2.6 pups per litter (Fig. 3.A). Additionally, of the 9 *Wnk1*$^{d/d}$ mice which survived to the end of the breeding trial, 2 never delivered, 3 only delivered one litter, and no mouse delivered beyond 3 litters (Fig. 3.A and Table S1). The average litter size was also significantly smaller, averaging 2.4 pups per litter in these mice, compared to 7.0 in the control *Wnk1*$^{f/f}$ mice (Fig. 3.B). While the *Wnk1*$^{f/f}$ mice bred consistently, producing the last litters in or after the twentieth week of the trial with only one exception, 5 of the 7 *Wnk1*$^{d/d}$ mice which reproduced stopped breeding before the 15th week (Fig. 3.C), indicating that there was premature loss of fertility. This loss of fertility was, however, not due to a progressive decrease in reproductive capacity, as demonstrated by the significant smaller size of the first litters produced by the Wnk1$^{d/d}$ mice compared to their control siblings (Fig. 3.D). Taken together, these results illustrated compromised ability to support pregnancy and premature sterility with uterine loss of WNK1.

We next examined whether the subfertile phenotype was associated with an implantation defect in the *Wnk1*$^{d/d}$ mice. Dams were euthanized on GD 4.5, and embryo implantation was visualized by Evans blue dye staining. As expected, 84.2% of the control mice successfully permitted embryo implantation on GD 4.5 while the remaining 15.8% had no embryos present in the uterus

(Fig. 3.E, top panel and Fig. 3.F). Significantly fewer of the mated *Wnk1*$^{d/d}$ mice were able to form implantation sites on GD 4.5 (29.4%; $p = 0.0019$); however, 52.9% of the mice harboured fertilized embryos inside the uterus (Fig. 3.E, top panel and Fig. 3.F). Examination of the uterus on GD 5.5 showed 76.9% of the *Wnk1*$^{d/d}$ mice with implantation sites which is, at this time point, comparable to their *Wnk1*$^{f/f}$ control littermates (Fig. 3.E, bottom panel). Histological examination showed that the control *Wnk1*$^{f/f}$ mice had already degraded the epithelium, enabling the embryo to invade the underlying stroma (Fig. 3.G, left), while *Wnk1*$^{d/d}$ uteri had intact uterine epithelium at this time point with the embryo trapped inside the luminal space (Fig. 3.G, right). These findings demonstrate that implantation is severely delayed in in the *Wnk1*$^{d/d}$ mice.

The *PGR*^{Cre} mouse model also causes recombination in the ovaries and pituitary, therefore we next evaluated the comtribution of these tissues to the WNK1 phenotype. Ovarian function was evaluated by assaying ovulation and ovarian steroid hormone levels. The mice were subjected to superovulatory regimen of gonadotropins, followed by mating to wildtype male mice, and euthanized on GD 1.5 to simultaneously monitor fertilization of the oocytes. We found a subtle albeit non-significant decrease in the number of 2-cell embryos produced by the *Wnk1*$^{d/d}$ dams indicating that ovulation and fertilization was not affected (Fig. S2.A). Additionally, serum estradiol (E_2) and progesterone (P_4) levels were similar between the *Wnk1*$^{f/f}$ and *Wnk1*$^{d/d}$ mice on GD 4.5 (Fig. S2.B and C), demonstrating that the pituitary and ovaries were functional and able to produce and maintain hormone levels. Therefore, the main contributing factor for the delayed implantation was not a malfunction of the pituitary-ovarian axis.

Prerequisites for uterine receptivity are the production of leukemia inhibitory factor (LIF) from the uterine glands, and the cessation of epithelial proliferation prior to implantation on GD 3.5 (22, 23); as well as suppression of epithelial PGR expression during implantation on GD 4.5 (24). Hence, we examined the uterus to see whether the delayed implantation was associated with impairment of those parameters. *Lif* expression on GD 3.5 was similarly induced in the *Wnk1$^{f/f}$* and *Wnk1$^{d/d}$* mice, suggesting that aberrant *Lif* expression was not the cause of disrupted implantation (Fig. 3.H). In the control mice, there was little to no expression of KI67 and PGR in the luminal epithelium on GD 4.5, as expected (Fig. 3.I). The *Wnk1$^{d/d}$* mice, however, maintained the expression of both proteins during the window of implantation (Fig. 3.I), demonstrating that crucial implantation-associated molecular events were deregulated in the *Wnk1$^{d/d}$* mice.

Abnormal embryo development and increased resorption in Wnk1$^{d/d}$ mice

Interestingly, of the 29.4% mated *Wnk1$^{d/d}$* mice with embryo implantated at the expected GD 4.5, the number of implantation sites were similar to their *Wnk1$^{f/f}$* control littermates (Fig. 4.A). However, the number of implantation sites present on GD 5.5 was significantly lower in the *Wnk1$^{d/d}$* mice indicating that the delay in implantation is associated with reduced number of implantation sites (Fig. 4.B and C). Additionally, spacing between the implantation sites in the *Wnk1$^{d/d}$* mice were irregular whereas the implantation sites observed in the *Wnk1$^{f/f}$* mice were evenly distributed (Fig. 4.C). This is supported by a significant increase in the standard deviation of inter-implantation sites distance in *Wnk1$^{d/d}$* uteri compared to *Wnk1$^{f/f}$* uteri (Fig. 4.D). For the *Wnk1$^{d/d}$* mice that were able to implant promptly, implantation spacing was more evenly distributed (Fig. 3.F), suggesting that the delay may impact both implantation numbers and spacing. Examination of the uterus and embryo during mid-pregnancy (GD 8.5) further demonstrated that the *Wnk1$^{d/d}$* mice carried either resorbed embryos (Fig. 4.E, middle) or abnormally formed decidual masses (Fig. 4.E, right), compared to the normally sized decidual masses observed in the control mice (Fig. 4.E, left). Moreover, we also observed multiple embryos within one decidual zone (Fig. 4.E, right), possibly from the cluttered/delayed implantation.

Morphology was evaluated by examining the cross sections through the center of the decidual mass, which showed that the *Wnk1*$^{f/f}$ mice have vascularized and initiated placentation (Fig. 4.F, black arrows and dashed lines, respectively), both of which were lacking in the *Wnk1*$^{d/d}$ uteri. Ultrasound scans demonstrated decreased gestation sac size (Fig. 4.G and H) and decreased embryo size at both GD 8.5 and GD 10.5 (Fig. 4.G and I). By GD 12.5, embryo resorption was frequently observed in the *Wnk1*$^{d/d}$ mice (Fig. 4.G). Collectively, these findings demonstrate that uterine WNK1 ablation led to abnormal implantation and negatively impacted embryo development, resulting in the compromised pregnancy outcome and subfertility.

Loss of uterine WNK1 elevated AKT signaling

To fully characterize the molecular mechanisms underlying the loss of WNK1 induced-implantation defect, we next examined global gene expression profile by RNA-seq in the uterus during receptivity. To ensure that the analysis was conducted only on the maternal uterine tissues and not the embryos, we used vasectomized wildtype males to induce pseudopregnancy in the *Wnk1*$^{f/f}$ and *Wnk1*$^{d/d}$ mice. Pregnancy was confirmed by serum progesterone levels on pseudopregnancy day (PPD) 4.5 (Table S2). In total, there were 14,423 and 14,337 genes expressed in the *Wnk1*$^{f/f}$ and *Wnk1*$^{d/d}$ uterus, respectively; of which 14,024 were expressed in both. The transcriptomes were subjected to principle component analysis (PCA) as a measure of quality control, which segregated according to genotype indicating that the samples were well-characterized by genotype (Fig. S3). Using a defining threshold of *q*-value under 0.05 for significance and fold change (FC) over 1.5 as differential expression, we identified 1,727 significantly and differentially expressed genes (DEGs) in the *Wnk1*$^{d/d}$ uterus during receptivity (Table S3). We then conducted detailed analyses to characterize the molecular alterations associated with uterine *Wnk1* ablation using the Database for Annotation, Visualization and Integrated Discovery (DAVID) bioinformatic database and Ingenuity Pathway Analysis (IPA).

Biological processes associated with the DEGs were adhesion, cell movement and locomotion, inflammation and blood vessel development (Table S4). Many important molecular functions associated with implantation were also deregulated in the *Wnk1*$^{d/d}$ uteri, such as cell proliferation and apoptosis, Notch signaling, cell differentiation, epithelial to mesenchymal transition (EMT), cytokine production, and response to estrogen. Prediction of upstream regulator activity further showed altered activity for many important receptivity mediators, including the suppression of JAG, HEY2, PTEN and SERPINE1 (Fig. 5.A). On the other hand, TGFB1, ERBB2, AKT, estrogen, ERK, MUC1 and KLF5 were predicted to show increased activity (Fig. 5.A, for the complete list see Table S5). As WNK1 is a kinase, we next examined the alterations in the kinase phosphorylation network. Image-based phosphokinase array was employed to evaluate the phosphorylation status of multiple kinases in the uterus during receptivity (Fig. 5.B and C). Loss of WNK1 altered the phosphorylation of TOR (MTOR), SRC, PRAS40 (AKT1S1), JNK, AMPKA1 (PRKAA1), GSK3A/B (GSK3A and GSK3B) and AKT (Fig. 5.B and C, all kinases with > 2 FC in phosphorylation are shown in Fig. S4.A). The phosphorylation of AKT, GSK3A/B and PRAS40 were independently validated via western blotting (Fig. S4.B) and all showed elevated phosphorylation in *Wnk1*$^{d/d}$ uteri during receptivity. Interestingly, AKT has been identified as an activated upstream regulator by IPA, which coincided with its increased phosphorylation. This was confirmed in both the epithelium and the stroma via IHC (Fig. 5.D). Indeed, we found that in the control mice, phosphorylation of AKT was suppressed as the mice transitioned into the receptive phase from GD 3.5 to PPD 4.5, however, the *Wnk1*$^{d/d}$ mice maintained high AKT phosphorylation both prior to and during receptivity (Fig. 5.E).

The AKT-regulated transcription factor FOXO1 is an indispensable mediator of implantation, as mice lacking uterine FOXO1 expression suffer infertility due to failed implantation (25). Interestingly, AKT is known to phosphorylate FOXO1 resulting in its nuclear exclusion and thereby inhibiting its transcriptional activity (26, 27). FOXO1 expression was assayed using IHC, and we found that indeed, there was a marked decrease in its nuclear form in both the luminal epithelium and underlying stroma (Fig. 5.F). This is further confirmed by the increase in the levels of phosphorylated FOXO1 in the *Wnk1*$^{d/d}$ uteri (Fig. 5.G). As FOXO1 nuclear exclusion prevents its transcriptional activity, we compared WNK1-regulated genes and FOXO1-regulated genes in the uterus during the receptive phase (25). This revealed that roughly half of the FOXO1-regulated genes are also deregulated in *Wnk1*$^{d/d}$ uteri (Fig. 5.H), and strikingly, 90% of those genes were deregulated in the same direction under WNK1 and FOXO1 deficient conditions – these included known implantation and decidualization associated genes such as *Msx2*, *Wnt5a* and *Muc1* (Fig. 5.I, Table S3, and Vasequez *et al*., 2018 (25, 28-30)). These findings indicate that uterine loss of WNK1 led to elevated AKT phosphorylation and, in turn, increased FOXO1 phosphorylation and nuclear exclusion hence altering expression of FOXO1-regulated genes.

WNK1 regulates FOXO1 localization via AKT, which is associated with decreased PP2A expression and activity

We next examined whether the WNK1-AKT-FOXO1 regulatory axis was maintained in human endometrial HEC1A (epithelial) and THESC (stromal) cells. WNK1 protein attenuation using small interfering RNA against *WNK1* (*siWNK1*) induced AKT and FOXO1 phosphorylation in both cell lines (Fig. 6.A). In order to test whether AKT facilitated FOXO1 localization downstream of WNK1, we next treated these cells with an AKT inhibitor, GDC0941, and examined whether it could rescue WNK1 ablation-induced phosphorylation and nuclear exclusion of FOXO1. FOXO1 localization clearly decreased in the nucleus of both cells after transfection with *siWNK1* (Fig. 6.B, panels 1 VS 2, and 4 VS 5). However, when the *siWNK1* transfected cells were treated with GDC0941, nuclear FOXO1 was readily restored (Fig. 6.B, panels 3 and 6). This suggested that WNK1 inhibition-induced nuclear exclusion of FOXO1 is mediated through AKT. This is further supported by the findings that AKT inhibition rescued WNK1 knock-down induced FOXO1 phosphorylation (Fig. 6.C). Interestingly, GDC0941 treatment reduced the phosphorylation of AKT and FOXO1 to a level that is lower than seen in the *siCTRL* transfected, untreated cells (considered basal level). As GDC0941 inhibits AKT through its upstream regulator PI3K (31), it is likely that PI3K lies upstream of WNK1 in regulating AKT. Indeed, none of the PI3K family members were impacted by WNK1 inhibition, including PIK3CA, PIK3CB, PIK3CG, as well as phosphorylation levels of PIK3R2 and PIK3R3 (Fig. 6.C). Similarly, no changes in the expression of these proteins was observed between the *Wnk1*$^{f/f}$ and *Wnk1*$^{d/d}$ mice during receptivity (Fig. 6.D).

Potential mechanisms by which WNK1 regulates AKT activity was explored by searching the upstream regulators predicted by IPA. Several candidates, including PTEN, PPP2CA, and sirolimus (rapamycin, Table S5) were identified. PTEN and PPP2CA are both phosphatases that regulate AKT phosphorylation, and both displayed repressed activities in the *Wnk1*$^{d/d}$ mice during receptivity (Z-scores of -2.079 and -1.195, respectively, Table S5). Sirolimus is a MTOR inhibitor, which was strongly inhibited (Z-score of -2.95, Table S5). We found that MTOR phosphorylation and PP2A subunits A and C were altered in the *Wnk1*$^{d/d}$ mice, while PTEN level was not significantly different (Fig. 6.E). This finding suggested that increased AKT phosphorylation in the *Wnk1*$^{d/d}$ mice may be mediated through elevated MTOR or repressed PP2A activity. As MTOR is both a regulator and a substrate of AKT (32, 33), we examined whether WNK1 ablation-induced AKT phosphorylation is mediated through MTOR. We inhibited MTOR activity using rapamycin and examined AKT/FOXO1 phosphorylation as well as FOXO1 localization as a readout of AKT activity. As shown in Fig. S5.A, rapamycin treatment did not reverse the nuclear exclusion of FOXO1 induced by WNK1 inhibition. Additionally, AKT and FOXO1 phosphorylation was not rescued by rapamycin treatment (Fig. S5.B). Similar results were observed in HEC1A cells where

WNK1 and MTOR double knock-down failed to rescue AKT and FOXO1 phosphorylation (Fig. S5.C). Thus, MTOR is likely not the WNK1 mediator controlling AKT activity, and its elevated phosphorylation is a result of elevated AKT activity, rather than its cause.

WNK1 regulates AKT phosphorylation through direct interaction with PPP2R1A

We next explored the possible regulatory link between WNK1 and PP2A/AKT using a non-biased WNK1 immunoprecipitation-mass spectrometry (IP-MS) approach to identify WNK1 binding partners. Successful WNK1 IP was confirmed by examining the lysate for WNK1 expression after immunoprecipition using a rabbit IgG (negative control) or WNK1 targeting antibody from HEC1A cells (Fig. S6), and the peptides identified by mass-spectrometry are listed in Table S6. Amongst those were peptides belonging to WNK1 itself, as well as a known WNK1 substrate, oxidative stress responsive kinase 1 (OXSR1/OSR1) (12), confirming the validity of the pull-down results (Table S6).

Putative WNK1 binding proteins included Wnt regulators (OFD1 and CCDC88C), chromosome modulating and DNA repair proteins (SMCA1, KIF11, FANCI, RAD50 and SLC25A5), proteins associated with the endoplasmic reticulum and ribosomal functions (UGGT1, SEC23A, HYOU1, EMC1, AIFM1, HM13, SCFD1) as well as the mitochondria (AIFM1, SLC25A5). Of particular interest were the components of protein phosphatase complexes PP2A (PPP2R1A), and PP6 (PPP6R3), as both are known AKT regulators (34, 35). Since the enzymatic activity of PP2A was predicted by IPA as repressed in the *Wnk1*$^{d/d}$ mice (PPP2CA, Table S5), we postulated that interaction between WNK1 and PPP2R1A (the alpha isoform of the scaffold subunit A of PP2A) impact PP2A activity. In order to confirm the interaction of WNK1 and PPP2R1A, a YFP-tagged WNK1 (c4161, Fig. S7) was expressed in HEC1A cells, then immunoprecipitated using a YFP nanobody, followed by detection for PPP2R1A in the pulldown. We first confirmed that c4161 transfection induced exogenous WNK1 expression when compared to the control cells transfected with YFP only expressing construct (cYFP, Fig. 7.A). WNK1 was subsequently detected in the lysate immunoprecipitated for YFP (Fig. 7.B, upper panel), which co-immunoprecipitated with PPP2R1A (Fig. 7.B, middle panel).

We next explored the biological implications of this WNK1-PPP2R1A interaction. The PP2A phosphatase complex is comprised of the scaffold subunit A with 2 isoforms, the regulatory subunit B with 13 isoforms and the enzymatic subunit C with 2 isoforms. As shown earlier, uterine WNK1 ablation led to decreased protein levels of subunits A and C (Fig. 6.E), yet RNA-seq showed no alteration in transcription of the 4 genes encoding these 2 subunits (*Ppp2ca*, *Ppp2cb*, *Ppp2r1a* and *Ppp2r1b*) in the *Wnk1*$^{d/d}$ mice. It has been reported that the stability of the PP2A subunits depends on their association with each other (36). Hence, reduced subunit levels could be an indication that the complexing capacity of the subunits were reduced in the absence of WNK1, leading to their degradation. We therefore postulated that the WNK1-PPP2R1A interaction is necessary for the association of the PP2A subunits. To test this idea, we examined the levels of PPP2R1A, total PP2A subunits A and C in WNK1 knock-down HEC1A cells, and accordingly found their reduced levels upon WNK1 inhibition (Fig. 7.C). Lastly, to validate that PP2A mediates AKT/FOXO1 signaling, we inhibited *PPP2R1A* expression in HEC1A cells using siRNA, and examined the components of the PP2A-AKT-FOXO1 signaling axis. As expected, PPP2R1A knock-down caused a reduction in total subunits A and C of PP2A (Fig. 7.D). Interestingly, AKT phosphorylation was selectively induced on threonine 308, but not serine 473 after PPP2R1A knock-down (Fig. 7.D). This nonetheless, translated to elevated FOXO1 phosphorylation, indicating that loss of PP2A activity-induced AKT phosphorylation on this residue alone is sufficient to increase FOXO1 phosphorylation (Fig. 7.D). These findings confirmed that in endometrial cells, WNK1 controls AKT activity through modulating its phosphorylation, which is partially mediated through PP2A (Fig. 7.E). As such, loss of WNK1 led to decreased PP2A activity and increased AKT phosphorylation, resulting in the pathological outcomes associated with AKT hypersignaling such as hyperplasia and FOXO1 deregulation (Fig. 7.E, blue and red arrows).

DISCUSSION

Reproductive biology has relied profoundly on transcriptomic analyses to identify novel players that may serve crucial functions in the regulation of fertility. While this approach has uncovered many key components in the reproductive tract, it is unable to detect alterations at the proteomic level, such as post translational modifications (PTMs). In many cases, the PTMs control protein activity and stability, and hence are the actual determinants of functional output. Through a proteomic approach, we identified WNK1 as a potential regulator of uterine biology with previously unreported reproductive functions (2).

In this study, we explored this futher by examining the *in vivo* function of WNK1, and we demonstrate here that loss of WNK1 led to hyperplasia, adenomyosis-like features and impaired implantation. We show for the first time that WNK1 robustly represses AKT activity and that loss of WNK1 led to increased AKT phosphorylation and signaling. This was evident through the increased MTOR and FOXO1 phosphorylation (26, 27, 33), resulting in nuclear exclusion of the latter and disrupted embryo implantation (25). Although both uterine WNK1 and FOXO1 deleted mice shared phenotypic similarity of implantation impairment, the two mouse models do not completely phenocopy each other. Ablation of WNK 1 resulted in chronical epithelial hyperplasia and adenomyotic glands, which were absent with FOXO1 ablation. Furthermore, while uterine loss of WNK1 and FOXO1 shared a commone transcriptomic footprint, each had a unique set of altered genes. Specifically, WNK1 regulated an additional 1,414 genes accounting for the epithelial hyperplasia and myometrial invasion of the glands which were not observed in the FOXO1 mice (25).

AKT is well known for promoting cell proliferation and is a target in anti-cancer therapy (37), which is supported by our observation that *Wnk1*$^{d/d}$ mice displayed epithelial hyperplasia resulting from escalated proliferation. Evidence has also shown a link between adenomyosis and estrogen induced AKT overactivity (38). Although not the focus of this work, the cellular changes and molecular events associated with WNK1 deficiency induced adenomyotic gland invasions seems to parallel observations made in humans, including excessive ECM deposition, elevated *Moesin* expression and AKT hypersignaling (19, 21). In the future, *Wnk1*$^{d/d}$ mice could serve as an ideal model system to study adenomyosis which affects a significant proportion of the population (39). Interestingly, there are evidence in literature showing that WNK1 is a substrate of AKT in other cellular and animal systems (40, 41). We observed a reduction in WNK1 phosphorylation after AKT inhibition in HEC1A and THESC cells (data not shown), suggesting that AKT could reciprocally interfere with WNK1 activity. These, together with our demonstration that WNK1 inhibits AKT phosphorylation and activity in endometrial cells suggest that the WNK1-AKT relationship involves a negative feedback and is likely more complex than previously thought.

Given that 30% of the *Wnk1*$^{d/d}$ mice were able to implant promptly with normal numbers of embryos, we rarely observed normal sized litters from these mice. This suggested that there must exist other impairments in subsequent pregnancy development accounting for the compromised fertility. The significant proportion of *Wnk1*$^{d/d}$ mice succumbing to pregnancy complications, including death near term and dystocia which indicated poor support of pregnancy and impaired uterine muscle contractility. This could be attributed to impaired decidualization – indeed, our previous *in vitro* study demonstrated that WNK1 is a regulator of decidualization (3). We did not extensively characterize decidualization in this study due to the preceding implantation defect – which complicates decidualization data interpretation. However, transcriptomic analysis identified alterations in several decidualizing regulators including Notch (HEY2 and JAG2), ERK and MUC signaling (42-44). Therefore, we are confident in speculating that loss of WNK1 likely negatively impacted decidualization *in vivo*. Additionally, the premature loss of fertility in those mice that survived to the end of the breeding trial suggested that the postpartum tissue repair and remodeling may also be impacted by loss of WNK1. Interestingly, Zhu *et al*. reported on the AKT dependent endometrial stromal cell repair in humans (45), providing a possible explanation for the premature sterility.

We identified a regulatory link between WNK1 and AKT with PP2A as the intermediate. Here, the loss of WNK1 reduced PP2A subunits A and C as well as PP2A phosphatase activity in endometrial cells of both humans and mice. A possibility is that WNK1 facilitates the binding of the subunits, resulting in PP2A complex binding and stabilization (36). Mechanistically, WNK1 directly interacts with PPP2R1A and hence this interaction may be crucial for PP2A complex formation, however, further experimentation will be necessary to test this hypothesis. It is worth noting that there must be additional mechanisms through which WNK1 is repressing AKT, as *PPP2R1A* knock-down in human cells restored only the phosphorylation on T308. However, WNK1 ablation induced phosphorylation on both T308 and S473.

As above mentioned, uterine ablation of WNK1 exhibited pleiotropic effects including epithelial hyperplasia and adenomyotic features. Although neither is cancerous, both are progressive conditions which may lead to malignant transformation (46, 47). Functional interpretation of the transcriptome reiterated this, where many cancer development and progression associated signaling pathways were altered in the *Wnk1*$^{d/d}$ uteri, including elevated TGFB, AKT and estrogen (47-50). Strikingly, a recurrent mutation of *Ppp2r1a* is associated with serous endometrial carcinoma (51, 52), and this mutation has been found to impact oncogenic signaling through a dominant negative effect (53). Although we demonstrate here that WNK1 positively regulate PP2A activity and propose a possibility that WNK1 could be associated with endometrial cancer, its exact role in endometrial cancer is yet unknown and worth exploring. Interestingly, there exist a known *WNK1* mutation in humans which causes *WNK1* overexpression and no impact on reproduction health has been reported. Nonetheless, investigating the activity of WNK1 in human endometrial cancers would shed light on its potential role in this disease. In summary, we demonstrate that WNK1 is critical in maintaining normal uterine morphology, mediating epitheial homeostasis and implantation and may play a potential role in human endometrial pathogenesis.

Methods

Generation of transgenic mice

The *Wnk1*$^{f/f}$ mice with the insertion of *loxP* sites into the 5’ and 3’ region of exon 2 were provided by Dr CL Huang (University of Iowa Healthcare, Iowa, IA) (14). The *Wnk1*$^{f/f}$ mice were crossed to mice carrying *Cre* under the control of the progesterone receptor (PGR^{Cre}) to generate conditional uterine *Wnk1* ablated mice (*Wnk1*$^{d/d}$, Fig. S1) (16).

Fertility trial

Seven to eleven-week old *Wnk1*$^{f/f}$ and *Wnk1*$^{d/d}$ mice were housed with wildtype C57BL/6J or CD1 males for a period of 6 months. The mice were monitored daily for pregnancy and delivery. Upon the first observation of delivery, the total number of pups were counted.

Implantation determination and pseudopregnancy

Virgin mice of age 6-10 weeks were housed with wildtype C57BL/6J males, and monitored each morning until vaginal plug is observed. The first noon following the observation of the vaginal plug was defined as GD 0.5. Mice were anesthetized by isoflurane inhalation on GD 4.5 and 5.5, followed by retro-orbital administration of 200 µL of 1% Evans blue dye to visualize the implantation status after euthanization. For mice sacrificed on GD 4.5 and showed no visible implantation site, uterine horns were flushed with PBS and the eluant was examined under brightfield microscope to determine presence of blastocysts. Uterine horns were fixed for 48 hours in 4% PFA for histology and IHC, or flash-frozen for RNA and protein extraction. For RNA-seq, pseudopregnancy was induced by mating the females to vasectomized wildtype male mice, and all procedures were conducted as described above.

Superovulation assay

Three-week old virgin *Wnk1*$^{f/f}$ and *Wnk1*$^{d/d}$ mice were subjected to a superovulation regimen, which consisted of pregnant mare's serum gonadotropin (5 IU, i.p.) (493-10-2.5, Lee Biosolutions), followed by human chorionic gonadotropin (5 IU, i.p.) (869031, EMD Millipore) 48 hours later. Mice were placed with wildtype CD1 males overnight. Mating was confirmed by presence of vaginal plug the next morning (GD 0.5), and mice were euthanized on GD 1.5 for oviduct flushing. The number of embryos was determined by counting under a brightfield microscope.

Serum collection

On GD or PPD 4.5, mice were anesthetized by intraperitoneal administration of Fetal Plus (1mg/10g body mass) and whole blood was collected via retro-orbital puncture. Serum was collected by allowing the blood to clot at room temperature (RT) for 30 minutes, then centrifuged at 1000G for 10 minutes at 4^{O}C. Hormone assays included estradiol (ES180S-100, Calbiochem ELISA) and progesterone (IB79105, IBL ELISA). These were conducted by the Ligand Core Laboratory of University of Virginia, Center for Research in Reproduction.

High frequency ultrasound imaging

On GDs 8.5, 10.5 and 12.5, high frequency ultrasound imaging was used to evaluate the uterus and embryo development. Dams were anesthetized by isoflurane inhalation and placed onto an electric heating pad to maintain body temperature. Abdominal hair was removed using depilatory cream (Nair$_{TM}$ Church & Dwight Co), and eye lubricant was applied to prevent desiccation. Dams were manipulated into a supine position for the scan while heart rate and body temperature were continuously monitored. Images were visualized and captured using the VisualSonics VevoR 2100 Imaging System with a 550s scan head (Fujifilm VisualSonics Inc., Toronto, ON) at 55 megahertz.

Tissue processing, histology, immunohistochemical and immunofluorescence staining

After PFA fixation, tissues were placed in 70% ethanol for a minimum of 48 hours, followed by dehydration, paraffin embedding and sectioning to 5 µm thickness. Sections were deparaffinized by 3 serial incubations in Citrisolv clearing agent (22-143-975, ThermoFisher), and rehydrated through decreasing ethanol dilutions. Histological sections were subjected to hematoxylin and eosin and Masson's trichrome staining, followed by dehydration through increasing ethanol dilutions, incubation in Citrisolv before mounting. For IHC, sections were subjected to antigen retrieval after rehydration using the Vector Labs Antigen Unmasking Solution as per manufacturer's instructions (H-3300, Vector Laboratories). Blocking of endogenous peroxidase was performed by treating the sections with 3% H_2O_2 for 10 minutes at RT. Tissues were blocked in 5% normal donkey serum (NDS) for 60 minutes, then incubated with primary antibody at 4^{O}C overnight. The slides were washed twice in PBS, and secondary antibody diluted in 1% w/v bovine serum albumin (BSA) was applied. The ABC reagent was applied to tissue according to the manufacturer's instructions (PK-6100, Vector Laboratories). Signals were developed using the Vector Labs DAB ImmPACT Staining Kit (SK-4105, Vector Laboratories). Finally, the tissue sections were counterstained with hematoxylin and dehydrated through increasing ethanol concentration, followed by Citrisolv incubation and mounting. For immunofluorescence, tissue sections were subjected to antigen retrieval as described above, then blocked in 0.4% v/v Triton

X-100, 1% BSA and 5% NDS for 30 minutes followed by overnight incubation in primary antibody prepared in 0.4% Triton X-100/PBS at 4^{O}C. Sections were washed in PBS and incubated with secondary antibodies diluted in 0.4% Triton X-100/PBS for 90 minutes. Finally, slides were washed 3 times in PBS, and coverslipped in DAPI containing mounting medium (H-1400, Vector Laboratories). Details of antibodies used in this study are provided in Table S7.

RNA extraction and cDNA conversion

Frozen tissues were disrupted in TRIzol by bead milling, followed by 2 aqueous phase separations using 1-Bromo-3-chloropane and chloroform. Pure ethanol was added to the aqueous layer, and the RNA was extracted using the Qiagen RNEasy RNA mini prep kit columns as per manufacturer's instructions (74104, Qiagen). Resulting RNA concentration and quality were determined using NanoDrop ND-1000. cDNA was generated by reverse transcription using the M-MLV Reverse Transcriptase (28025013, ThermoFisher) following the manufacturer's instructions.

qRT-PCR

qRT-PCR was performed using the SsoAdvancedTM Universal SYBR Green Supermix (1725274, Bio-Rad) with the following primers (from 5' to 3', F = forward and R = reverse): *Wnk1* – AGGCAGAGATTCAAAGAAGAGG (F) and CCCAGGAATCATAGAATCGAACA (R); *Msn* – CCATGCCGAAGACGATCA (F) and CCAAACTTCCCTCAAACCAATAG (R); and *Foxa2* – GAGACTTTGGGAGAGCTTTGAG (F) and GATCACTGTGGCCCATCTATTT (R). *Lif* expression was determined using the Taqman Master Mix (Life Technologies) and Taqman probes (Applied Biosystems). The Delta delta Ct values were calculated using 18S RNA control amplification results to acquire the relative mRNA expression for each gene.

RNA-sequencing

For each mouse, 1 µg of uterine RNA was sent to the NIH Intramural Sequencing Center to create a library using the TruSeq RNA Kit (Illumina) following the manufacturer's instructions. The libraries were sequenced with a HiSeq 2000 System (Illumina). The raw RNA reads (75 nt, paired-end) were processed by filtering with average quality score greater than 20. Reads that passed the initial processing were aligned to the mouse reference genome (mm10; Genome Reference Consortium Mouse Build 38 from December 2011) using TopHat version 2.0.4 (54). Expression values of RNA-seq were expressed as fragments per kilobase of exon per million fragments (FPKM). Differential expression was calculated using Cuffdiff function from Cufflinks version 2.2 (55). Transcripts with the average FPKM > 1 in at least one group, q-value < 0.05 and at least 1.5-fold difference in FPKM were defined as DEGs. Data for this publication has been deposited in NCBI's Gene Expression Omnibus and are accessible through GEO Series accession number GSE144802. Functional annotation for the differentially expressed genes derived from RNA-seq were analyzed by IPA and DAVID (56).

Human phospho-kinase antibody array

Site specific phosphorylation levels of 43 kinases were measured using the Human Phospho-Kinase Array, HPA, Kit (ARY003B, R&D Systems) according to the manufacturer's instructions with the experimental design as described below. Mice were euthanized on PPD 4.5 with uterine tissues flash frozen and stored at -80^{O}C. Lysate were extracted independently from 6 mice per group by bead milling in the HPA lysis buffer, and protein concentrations were determined using the BCA Kit (23225, Pierce). Equal amounts from each mouse were pooled in each group (to a total of 900 µg), and the remaining steps followed the standard HPA protocol. Signal intensity was quantified by ImageJ (57). Images shown in the main figure were chosen to allow visualization of maximal difference between *Wnk1*$^{f/f}$ and *Wnk1*$^{d/d}$ mice for selected kinases, but quantification was performed using blots in the non-saturation range.

Protein extraction from uterine tissues and protein expression analysis

Tissues were homogenized in RIPA Lysis and Extraction Buffer (89900, ThermoFisher) supplemented with protease inhibitor cocktail (11836170001, Roche Diagnostics) and phosphatase inhibitor cocktail (4906837001, Roche Diagnostics), then centrifuged at 10,000G for 10 minutes at 4^{O}C, and pellets discarded. Protein concentrations were measured using the BCA Kit (23225, Pierce). Heat denatured protein samples were resolved using 7.5%, 10% or gradient 4-20% Criterion Tris-HCl precast gels (Bio-Rad), followed by transferring using the Trans-Blot Turbo Transfer System (Bio-Rad), as according to the manufacturer's instructions. PVDF and nitrocellulose membranes were used for target proteins > 200 kDa and < 200 kDa, respectively. After transfer, the membranes were blocked in 5% w/v non-fat milk or BSA. Membranes were incubated with primary antibody at 4^{O}C overnight, washed three times and incubated in secondary antibody the next day. Finally, membranes were washed another 3 times, and depending on the expected signal strength, different peroxidase chemiluminescent substrates were used: KPL LumiGLO^{R} (546101, Seracare), Clarity Western ECL Substrate (1705060, Bio-Rad), and Amersham ECL Prime Western Blotting Detection Reagent (RPN2232, GE Healthcare Life Sciences). Antibody sources and dilutions are summarized in Table S7. For each western blot, GAPDH or B-tubulin were detected as the loading control, and in cases where the target protein is in the same region as the loading control proteins, a duplicate gel was ran and transferred in parallel. For each set of samples, a representing GAPDH or B-tubulin blot is shown.

Tissue clearing and 3D reconstruction

Uterine tissues were fixed in 4% PFA for 16 hours, followed by 3 rinses in PBS. Tissues were incubated in hydrogel monomer solution AP40 (4% v/v acrylamide and 0.25% w/v VA-044 in PBS) for 72 hours at $4^{O}C$ protected from light. Oxygen was then removed in a chamber connected to vacuum and nitrogen, followed by incubation at $37^{O}C$ for 3 hours to initiate tissue-hydrogel hybridization. Hydrogel was removed from the tissues via 3 PBS washes, and tissues were subsequently incubated in 8% SDS prepared in PBS for 7 days at $37^{O}C$ with shaking, and the SDS solution replaced twice during incubation. Tissues were washed 5 times one hour in PBS and blocked in 5% NDS prepared in PBS/triton X-100 with 0.01% of sodium azide. The samples were incubated in primary antibody in 2% v/v NDS and 0.01% w/v sodium azide for 6 days at RT with constant rotation, followed by 5 one hour washes in 0.1% v/v Triton in PBS (PBS-T). Secondary antibody was similarly prepared and incubated for another 6 days at RT with constant rotation and protected from light, replacing antibody after 3 days. Finally, the samples were washed an additional 5 times one hour in PBS-T and incubated in Refractive Index Matching Solution (80% w/v Histodenz (D2158, Sigma-Aldrich) prepared in 0.02M phosphate buffer, pH7.5 with 0.1% Tween-20 and 0.01% sodium azide, refractive index = 1.46) for 1-3 days, and samples were mounted in fresh Reflective Index Mounting Solution using a 1 mm deep iSpacer (www.sunjinlabs.com). Details of antibodies used in this study are provided in Table S7.

Cell culture

Human endometrial epithelial cell line HEC1A and telomerase-transformed human endometrial stromal cells (THESC) were obtained from American Type Culture Collection (ATCC, Rockville, MD, USA). HEC1A cells were cultured in McCoy's 5A modified medium (16600082, Gibco) and the THSEC cells were maintained in DMEM/F12 (1:1) (11330-032, Gibco), both supplemented with 10% FBS (10437-028, Gibco) and 100 U/mL penicillin and 100 µg/mL streptomycin, unless otherwise stated.

siRNA transfection and drug treatments

Cells were transfected with siRNAs using the Lipofectamine RNAiMax transfection reagent (13778150, ThermoFisher) following the manufacturer's protocol. Cells were transfected with 24 – 72 nM siRNA in transfection medium supplemented with 2% charcoal-stripped FBS (12676-029, Gibco) for 24-48 hours before replacing with fresh growth medium. Proteins were harvested from cells 72 hours after transfection unless otherwise stated. The siRNAs used in this study were: nontargeting siRNA (*siCTRL*, D-001810-10-20, Dharmacon), *WNK1* targeting siRNA (*siWNK1*, L-005362-02-0005, Dharmacon), *MTOR* targeting siRNA (*siMTOR*, L-003008-00-0005, Dharmacon), and *PPP2R1A* targeting siRNA (*siPPP2R1A*, L-060647-00-0005, Dharmacon). AKT and MTOR inhibitors GDC0941 and rapamycin (S1065 and S1039, respectively, Selleckchem) were dissolved in DMSO, and cells were treated with 5 µM GDC 0941 and 10 – 40 µM rapamycin for 24 hours, while the control cells received equivalent volumes of DMSO.

Immunofluorescence of cultured cells

Cells were seeded in 4-chambered coverglass (155382, ThermoFisher) and following with siRNA transfection and/or drug treatment. Cells were rinsed in PBS, fixed in 4% PFA and permeabilized in 0.5% Triton X-100/PBS for 10 and 5 minutes, respectively. Cells were incubated in blocking buffer (5% v/v NDS, 0.2% v/v fish gelatin (G7765, Sigma-Aldrich), 0.2% v/v Tween-20 in PBS) for 30 minutes at 37^{O}C. Primary antibody was diluted in blocking buffer and added to the cells for 60 minutes, followed by secondary antibody for another 60 minutes; both incubation steps were performed at 37^{O}C in a humidified chamber. Finally, cells were rinsed 3 times with 0.2% Tween-

20/PBS and coverslipped using a DAPI containing mounting medium (H-1400, Vector Laboratories). Details of antibodies used in this study are provided in Table S7.

WNK1 Immunoprecipitation Mass-spectrometry

HEC1A cells were grown to 70% confluency, followed by collection using trypsin. Cells were washed 2 X in cold PBS, followed by resuspension in cell lysis buffer (50 mM Tris-HCl pH 7.5, 150 mM NaCl, 1 mM EDTA, 1% NP-40, 1% sodium deoxycholate, 0.1% SDS, with protease and phosphatase inhibitors added fresh to 1 X). Cells were incubated on ice for 10 minutes, followed by sonication on medium power (3 X 5 seconds). Lysate was centrifuged at 13,000G for 10 minutes at 4^{O}C. WNK1 targeting antibody was added at 1:100 to the supernatant, and incubated with rotation at 4^{O}C overnight. Prewashed beads (50% protein A and 50% protein G, 10002D and 10004D, respectively, ThermoFisher) were added to the immunocomplex and incubated for 30 minutes at RT with rotation. Beads were pelleted using a magnetic separation rack, followed by 3 washes in lysis buffer. Beads were heated to 100^{O}C with SDS buffer (150 mM Tris-HCl pH 6.8, 6% SDS, 0.3% BPB, 30% glycerol, 3% B-mercaptoethanol) for 5 minutes, before electrophoresis through a 7.5% Criterion Tris-HCl precast gel (Bio-Rad). Gel regions containing the proteins were excised and minced, and digests were performed with a ProGest robotic digester (Genomic Solutions) where the gel pieces were destained by incubation in 25 mM ammonium bicarbonate with 50% acetonitrile (v/v) twice for a total of 30 minutes. The gel pieces were dehydrated in acetonitrile, followed by drying under a nitrogen stream, and further incubated with 250 ng trypsin (Promega) for 8 hours at 37^{O}C. The digests were collected, and peptides were re-extracted three times. The extractions were pooled for each sample, lyophilized and resuspended in 20 µL 0.1% formic acid. The protein digests were analyzed by LC/MS on a Q Exactive Plus mass spectrometer (ThermoFisher) interfaced with a nanoAcquity UPLC system (Waters Corporation), and equipped with a 75 µm x 150 mm BEH dC18 column (1.8 µm particle, Waters Corporation) and a C18 trapping column (18 µm x 20 mm) with a 5 µm particle size at a flow rate of 400 nL/min. The trapping column was positioned in-line of the analytical column and upstream of a micro-tee union which was used both as a vent for trapping and as a liquid junction. Trapping was performed using the initial solvent composition. A volumn of 5 µL of digested sample was injected into the column, and peptides were eluted by using a linear gradient from 99% solvent A (0.1% formic acid in water (v/v)) and 1% solvent B (0.1%formic acid in acetonitrile (v/v)), to 40% solvent B over 60 minutes. For the mass spectrometry, a data dependent acquisition method was employed with an exclusion time of 15 seconds and an exclusion of +1 charge states. The mass spectrometer was equipped with a NanoFlex source and was used in the positive ion mode. Instrument parameters were as follows: sheath gas, 0; auxiliary gas, 0; sweep gas, 0; spray voltage, 2.7 kV; capillary temperature, 275^{O}C; S-lens, 60; scan range (m/z) of 200 to 2000; 2 m/z isolation window; resolution: 70,000; automated gain control (AGC), 2×10^5 ions; and a maximum IT of 200 ms. Mass calibration was performed before data acquisition using the Pierce LTQ Velos Positive Ion Calibration mixture (ThermoFisher). Peak lists were generated from the LC/MS data using Mascot Distiller (Matrix Science) and the resulting peak lists were searched using the Spectrum Mill software package (Agilent) against the SwissProt database. Searches were performed using trypsin specificity and allowed for one missed cleavage and variable methionine oxidation. Mass tolerance were 20 ppm for MS scans and 50 ppm for MSMS scans.

Generation of mammalian YFP-WNK1 expression constructs

The coding region of the WNK1 sequence (NM_014823.3) with attL sites and N-terminal TEV cleavage site was synthesized by GeneWiz Inc. and cloned into pUC57 (Kanamycin) plasmid. Gateway Cloning with LR Clonase II mix (ThermoFisher) was used to transfer the WNK1 sequence into the Vivid Colors pcDNA6.2/N-YFP vectors (ThermoFisher), which created the mammalian expression vectors with YFP fused to the N-terminal end of WNK1 (Fig. S7, c4161).

Co-Immunoprecipitation

HEC1A cells were transfected with cYFP or c4161 for 48 hours, followed by trypsinization, 3 washes and resuspension in lysis buffer (50 mM Tris pH8.0, 400 mM NaCl, 0.1% NP-40 and 0.5 mM DTT, with protease and phosphatase inhibitors freshly added to 1 X). The lysate was incubated at 4^{O}C with rotation for 30 minutes, then centrifuged at 21,100G for 10 minutes. The supernatant was added to 1.5 volumes of 25% glycerol, followed by centrifugation at 21,100G for 10 minutes at 4^{O}C. Anti-GFP resin slurry was added to the supernatant and nutated for 1 hour at 4^{O}C. Beads were centrifuged at 1,000G for 5 minutes, 4^{O}C, followed by 6 washes in 100 µL of PBST in Bio-Spin columns (7326204, Bio-Rad). The bound immunocomplexes were eluted via 0.1 M glycine, pH 2.0, and eluent was neutralized using 2M Tris-HCl, pH 8.0.

Confocal Microscopy

All fluorescent images presented in this study were captured using the Zeiss LSM 780 UV confocal microscope.

Statistics

GraphPad Prism versions 7 and 8 were used for data analysis. Each set of data points were first subjected for normality test. Two-tailed student's *t* tests and Mann-Whiteney tests were performed for normally distributed data and non-normally distributed data, respectively. For % of mice with implantation post mating, Fisher's exact test was performed. In each case, a *p*-value less than 0.05 was considered as significant.

Study approval

This study was conducted according to the federal regulations regarding the use of human subjects. Procedures were approved by the following ethics committee: Institutional Review Board/Committee-A (IRB) of Greenville Health System under IRB file #Pro0000093 and Pro00013885 and the University of Chapel Hill at North Carolina IRB under file #: 05-1757. Written, informed consents were obtained from all patients prior to participation.

All animal studies were conducted in accordance with the Guide for the Care and Use of Laboratory Animals, as published by the National Institute of Health. Animal protocols were approved by the Animal Care and Use Committee (ACUC) of National Institute of Environmental Health Sciences (protocol numbers 2015-0012 and 2015-0023). The mice were housed with a maximum of 5 per cage with a 12-hour light and dark cycle, and fed irradiated Teklad global soy protein-free extruded rodent diet (Harlem Laboratories, Inc., Indianapolis, IN) and fresh water ad libitum. Euthanization was carried out by carbon dioxide inhalation followed by cervical dislocation. As there appear to be premature loss of fertility in the *Wnk1*$^{d/d}$ mice, all experiments were conducted following first mating of virgin mice, unless otherwise stated.

AUTHOR CONTRIBUTIONS

Conceptualization, R.A.C., S.P.W. and F.J.D.; Methodology, R.A.C. and F.J.D.; Validation, R.A.C.; Formal Analysis, R.A.C. and T.W.; Investigation, R.A.C.; Resources, S.L.Y., J.L., C.L.H. and F.J.D.; Data Curation, R.A.C. and T.W.; Writing – Original Draft, R.A.C.; Writing – Review & Editing, R.A.C. and F.J.D.;Visualization, R.A.C.; Supervision, F.J.D.; Project Administration, R.A.C. and F.J.D.; Funding Acquisition, F.J.D.

ACKNOWLEDGEMENTS

This work was supported in part by Intramural Research Program of the National Institute of Health (Z1AES103311-01 (F.J.D.)); the Eunice Kennedy Shriver National Institute of Child Health & Human Development (RO1 HD042311 (J.P.L)); and National Institute of Diabetes and Digestive and Kidney Diseases (RO1 DK111542 (C.-L.H)). The authors thank Dr Sheng Song for guidance on the CLARITY technique; Dr Nyssa Adams for conducting the initial breeding trial, Dr Carmen Williams and Dr Sophia Tsai for reviewing the manuscript. We appreciate support from the NIEHS animal facility, Knockout Mouse Core, Digital Imaging Core, the Epigenomics and DNA Sequencing Core, the Fluorescent Microscopy and Imaging Core, the Mass Spectrometry Research and Support Group, the Structural Biology Core of NIEHS for their support and guidance with specialized techniques, as well as the Ligand Assay and Analysis Core at the University of Virginia.

REFERENCES

1. Wang H, Dey SK. Roadmap to embryo implantation: clues from mouse models. Nature reviews Genetics. 2006;7(3):185-99.
2. Large MJ, Wetendorf M, Lanz RB, Hartig SM, Creighton CJ, Mancini MA, et al. The epidermal growth factor receptor critically regulates endometrial function during early pregnancy. PLoS genetics. 2014;10(6):e1004451.
3. Adams NR, Vasquez YM, Mo Q, Gibbons W, Kovanci E, DeMayo FJ. WNK lysine deficient protein kinase 1 regulates human endometrial stromal cell decidualization, proliferation, and migration in part through mitogen-activated protein kinase 7. Biology of reproduction. 2017;97(3):400-12.
4. Moore TM, Garg R, Johnson C, Coptcoat MJ, Ridley AJ, Morris JD. PSK, a novel STE20-like kinase derived from prostatic carcinoma that activates the c-Jun N-terminal kinase mitogen-activated protein kinase pathway and regulates actin cytoskeletal organization. The Journal of biological chemistry. 2000;275(6):4311-22.
5. Nagase T, Ishikawa K, Nakajima D, Ohira M, Seki N, Miyajima N, et al. Prediction of the coding sequences of unidentified human genes. VII. The complete sequences of 100 new cDNA clones from brain which can code for large proteins in vitro. DNA research : an international journal for rapid publication of reports on genes and genomes. 1997;4(2):141-50.
6. Xu B, English JM, Wilsbacher JL, Stippec S, Goldsmith EJ, Cobb MH. WNK1, a novel mammalian serine/threonine protein kinase lacking the catalytic lysine in subdomain II. The Journal of biological chemistry. 2000;275(22):16795-801.
7. Wilson FH, Disse-Nicodeme S, Choate KA, Ishikawa K, Nelson-Williams C, Desitter I, et al. Human hypertension caused by mutations in WNK kinases. Science (New York, NY). 2001;293(5532):1107-12.
8. Disse-Nicodème S, Achard JM, Desitter I, Houot AM, Fournier A, Corvol P, et al. A new locus on chromosome 12p13.3 for pseudohypoaldosteronism type II, an autosomal dominant form of hypertension. American journal of human genetics. 2000;67(2):302-10.
9. Lafreniere RG, MacDonald ML, Dube MP, MacFarlane J, O'Driscoll M, Brais B, et al. Identification of a novel gene (HSN2) causing hereditary sensory and autonomic neuropathy type II through the Study of Canadian Genetic Isolates. American journal of human genetics. 2004;74(5):1064-73.
10. Xu BE, Stippec S, Chu PY, Lazrak A, Li XJ, Lee BH, et al. WNK1 activates SGK1 to regulate the epithelial sodium channel. Proceedings of the National Academy of Sciences of the United States of America. 2005;102(29):10315-20.
11. Wade JB, Fang L, Liu J, Li D, Yang CL, Subramanya AR, et al. WNK1 kinase isoform switch regulates renal potassium excretion. Proceedings of the National Academy of Sciences of the United States of America. 2006;103(22):8558-63.
12. Anselmo AN, Earnest S, Chen W, Juang YC, Kim SC, Zhao Y, et al. WNK1 and OSR1 regulate the Na+, K+, 2Cl- cotransporter in HeLa cells. Proceedings of the National Academy of Sciences of the United States of America. 2006;103(29):10883-8.
13. Vitari AC, Deak M, Morrice NA, Alessi DR. The WNK1 and WNK4 protein kinases that are mutated in Gordon's hypertension syndrome phosphorylate and activate SPAK and OSR1 protein kinases. The Biochemical journal. 2005;391(Pt 1):17-24.
14. Xie J, Wu T, Xu K, Huang IK, Cleaver O, Huang CL. Endothelial-specific expression of WNK1 kinase is essential for angiogenesis and heart development in mice. The American journal of pathology. 2009;175(3):1315-27.
15. Xie J, Yoon J, Yang SS, Lin SH, Huang CL. WNK1 protein kinase regulates embryonic cardiovascular development through the OSR1 signaling cascade. The Journal of biological chemistry. 2013;288(12):8566-74.

16. Soyal SM, Mukherjee A, Lee KY, Li J, Li H, DeMayo FJ, et al. Cre-mediated recombination in cell lineages that express the progesterone receptor. Genesis (New York, NY : 2000). 2005;41(2):58-66.

17. Yang B, Treweek JB, Kulkarni RP, Deverman BE, Chen CK, Lubeck E, et al. Single-cell phenotyping within transparent intact tissue through whole-body clearing. Cell. 2014;158(4):945-58.

18. Arora R, Fries A, Oelerich K, Marchuk K, Sabeur K, Giudice LC, et al. Insights from imaging the implanting embryo and the uterine environment in three dimensions. Development (Cambridge, England). 2016;143(24):4749-54.

19. Ohara R, Michikami H, Nakamura Y, Sakata A, Sakashita S, Satomi K, et al. Moesin overexpression is a unique biomarker of adenomyosis. Pathology international. 2014;64(3):115-22.

20. Frantz C, Stewart KM, Weaver VM. The extracellular matrix at a glance. Journal of cell science. 2010;123(Pt 24):4195-200.

21. Kishi Y, Shimada K, Fujii T, Uchiyama T, Yoshimoto C, Konishi N, et al. Phenotypic characterization of adenomyosis occurring at the inner and outer myometrium. PloS one. 2017;12(12):e0189522.

22. Stewart CL, Kaspar P, Brunet LJ, Bhatt H, Gadi I, Kontgen F, et al. Blastocyst implantation depends on maternal expression of leukaemia inhibitory factor. Nature. 1992;359(6390):76-9.

23. Dey SK, Lim H, Das SK, Reese J, Paria BC, Daikoku T, et al. Molecular cues to implantation. Endocrine reviews. 2004;25(3):341-73.

24. Wetendorf M, Wu SP, Wang X, Creighton CJ, Wang T, Lanz RB, et al. Decreased epithelial progesterone receptor A at the window of receptivity is required for preparation of the endometrium for embryo attachment. Biology of reproduction. 2017;96(2):313-26.

25. Vasquez YM, Wang X, Wetendorf M, Franco HL, Mo Q, Wang T, et al. FOXO1 regulates uterine epithelial integrity and progesterone receptor expression critical for embryo implantation. PLoS genetics. 2018;14(11):e1007787.

26. Brunet A, Bonni A, Zigmond MJ, Lin MZ, Juo P, Hu LS, et al. Akt promotes cell survival by phosphorylating and inhibiting a Forkhead transcription factor. Cell. 1999;96(6):857-68.

27. Tang ED, Nunez G, Barr FG, Guan KL. Negative regulation of the forkhead transcription factor FKHR by Akt. The Journal of biological chemistry. 1999;274(24):16741-6.

28. Cha J, Bartos A, Park C, Sun X, Li Y, Cha SW, et al. Appropriate crypt formation in the uterus for embryo homing and implantation requires Wnt5a-ROR signaling. Cell reports. 2014;8(2):382-92.

29. Aplin JD, Meseguer M, Simón C, Ortíz ME, Croxatto H, Jones CJ. MUC1, glycans and the cell-surface barrier to embryo implantation. Biochemical Society transactions. 2001;29(Pt 2):153-6.

30. Daikoku T, Cha J, Sun X, Tranguch S, Xie H, Fujita T, et al. Conditional deletion of Msx homeobox genes in the uterus inhibits blastocyst implantation by altering uterine receptivity. Developmental cell. 2011;21(6):1014-25.

31. Folkes AJ, Ahmadi K, Alderton WK, Alix S, Baker SJ, Box G, et al. The identification of 2-(1H-indazol-4-yl)-6-(4-methanesulfonyl-piperazin-1-ylmethyl)-4-morpholin-4-yl-t hieno[3,2-d]pyrimidine (GDC-0941) as a potent, selective, orally bioavailable inhibitor of class I PI3 kinase for the treatment of cancer. Journal of medicinal chemistry. 2008;51(18):5522-32.

32. Malley CO, Pidgeon GP. The mTOR pathway in obesity driven gastrointestinal cancers: Potential targets and clinical trials. BBA clinical. 2016;5:29-40.

33. Dan HC, Ebbs A, Pasparakis M, Van Dyke T, Basseres DS, Baldwin AS. Akt-dependent activation of mTORC1 complex involves phosphorylation of mTOR (mammalian target of rapamycin) by IkappaB kinase alpha (IKKalpha). The Journal of biological chemistry. 2014;289(36):25227-40.

34. Kurosawa K, Inoue Y, Kakugawa Y, Yamashita Y, Kanazawa K, Kishimoto K, et al. Loss of protein phosphatase 6 in mouse keratinocytes enhances K-ras(G12D) -driven tumor promotion. Cancer science. 2018;109(7):2178-87.

35. Ye J, Shi H, Shen Y, Peng C, Liu Y, Li C, et al. PP6 controls T cell development and homeostasis by negatively regulating distal TCR signaling. Journal of immunology (Baltimore, Md : 1950). 2015;194(4):1654-64.

36. Seshacharyulu P, Pandey P, Datta K, Batra SK. Phosphatase: PP2A structural importance, regulation and its aberrant expression in cancer. Cancer letters. 2013;335(1):9-18.

37. Shariati M, Meric-Bernstam F. Targeting AKT for cancer therapy. Expert opinion on investigational drugs. 2019;28(11):977-88.

38. Xue J, Zhang H, Liu W, Liu M, Shi M, Wen Z, et al. Metformin inhibits growth of eutopic stromal cells from adenomyotic endometrium via AMPK activation and subsequent inhibition of AKT phosphorylation: a possible role in the treatment of adenomyosis. Reproduction (Cambridge, England). 2013;146(4):397-406.

39. Naftalin J, Hoo W, Pateman K, Mavrelos D, Holland T, Jurkovic D. How common is adenomyosis? A prospective study of prevalence using transvaginal ultrasound in a gynaecology clinic. Human reproduction (Oxford, England). 2012;27(12):3432-9.

40. Vitari AC, Deak M, Collins BJ, Morrice N, Prescott AR, Phelan A, et al. WNK1, the kinase mutated in an inherited high-blood-pressure syndrome, is a novel PKB (protein kinase B)/Akt substrate. The Biochemical journal. 2004;378(Pt 1):257-68.

41. Jiang ZY, Zhou QL, Holik J, Patel S, Leszyk J, Coleman K, et al. Identification of WNK1 as a substrate of Akt/protein kinase B and a negative regulator of insulin-stimulated mitogenesis in 3T3-L1 cells. The Journal of biological chemistry. 2005;280(22):21622-8.

42. Afshar Y, Jeong JW, Roqueiro D, DeMayo F, Lydon J, Radtke F, et al. Notch1 mediates uterine stromal differentiation and is critical for complete decidualization in the mouse. FASEB journal : official publication of the Federation of American Societies for Experimental Biology. 2012;26(1):282-94.

43. Lee CH, Kim TH, Lee JH, Oh SJ, Yoo JY, Kwon HS, et al. Extracellular signal-regulated kinase 1/2 signaling pathway is required for endometrial decidualization in mice and human. PloS one. 2013;8(9):e75282.

44. Zhang L, Patterson AL, Zhang L, Teixeira JM, Pru JK. Endometrial stromal beta-catenin is required for steroid-dependent mesenchymal-epithelial cross talk and decidualization. Reproductive biology and endocrinology : RB&E. 2012;10:75.

45. Zhu H, Jiang Y, Pan Y, Shi L, Zhang S. Human menstrual blood-derived stem cells promote the repair of impaired endometrial stromal cells by activating the p38 MAPK and AKT signaling pathways. Reproductive biology. 2018;18(3):274-81.

46. Yeh CC, Su FH, Tzeng CR, Muo CH, Wang WC. Women with adenomyosis are at higher risks of endometrial and thyroid cancers: A population-based historical cohort study. PloS one. 2018;13(3):e0194011.

47. Sobczuk K, Sobczuk A. New classification system of endometrial hyperplasia WHO 2014 and its clinical implications. Przeglad menopauzalny = Menopause review. 2017;16(3):107-11.

48. Daikoku T, Hirota Y, Tranguch S, Joshi AR, DeMayo FJ, Lydon JP, et al. Conditional loss of uterine Pten unfailingly and rapidly induces endometrial cancer in mice. Cancer research. 2008;68(14):5619-27.

49. Kriseman M, Monsivais D, Agno J, Masand RP, Creighton CJ, Matzuk MM. Uterine double-conditional inactivation of Smad2 and Smad3 in mice causes endometrial dysregulation, infertility, and uterine cancer. Proceedings of the National Academy of Sciences of the United States of America. 2019;116(9):3873-82.

50. Pavlidou A, Vlahos NF. Molecular alterations of PI3K/Akt/mTOR pathway: a therapeutic target in endometrial cancer. TheScientificWorldJournal. 2014;2014:709736.

51. Kuhn E, Wu RC, Guan B, Wu G, Zhang J, Wang Y, et al. Identification of molecular pathway aberrations in uterine serous carcinoma by genome-wide analyses. Journal of the National Cancer Institute. 2012;104(19):1503-13.

52. Zhao S, Choi M, Overton JD, Bellone S, Roque DM, Cocco E, et al. Landscape of somatic single-nucleotide and copy-number mutations in uterine serous carcinoma. Proceedings of the National Academy of Sciences of the United States of America. 2013;110(8):2916-21.

53. Haesen D, Abbasi Asbagh L, Derua R, Hubert A, Schrauwen S, Hoorne Y, et al. Recurrent PPP2R1A Mutations in Uterine Cancer Act through a Dominant-Negative Mechanism to Promote Malignant Cell Growth. Cancer research. 2016;76(19):5719-31.

54. Trapnell C, Pachter L, Salzberg SL. TopHat: discovering splice junctions with RNA-Seq. Bioinformatics (Oxford, England). 2009;25(9):1105-11.

55. Trapnell C, Williams BA, Pertea G, Mortazavi A, Kwan G, van Baren MJ, et al. Transcript assembly and quantification by RNA-Seq reveals unannotated transcripts and isoform switching during cell differentiation. Nature biotechnology. 2010;28(5):511-5.

56. Huang da W, Sherman BT, Lempicki RA. Systematic and integrative analysis of large gene lists using DAVID bioinformatics resources. Nature protocols. 2009;4(1):44-57.

57. Schneider CA, Rasband WS, Eliceiri KW. NIH Image to ImageJ: 25 years of image analysis. Nature methods. 2012;9(7):671-5.

FIGURES AND FIGURE LEGENDS

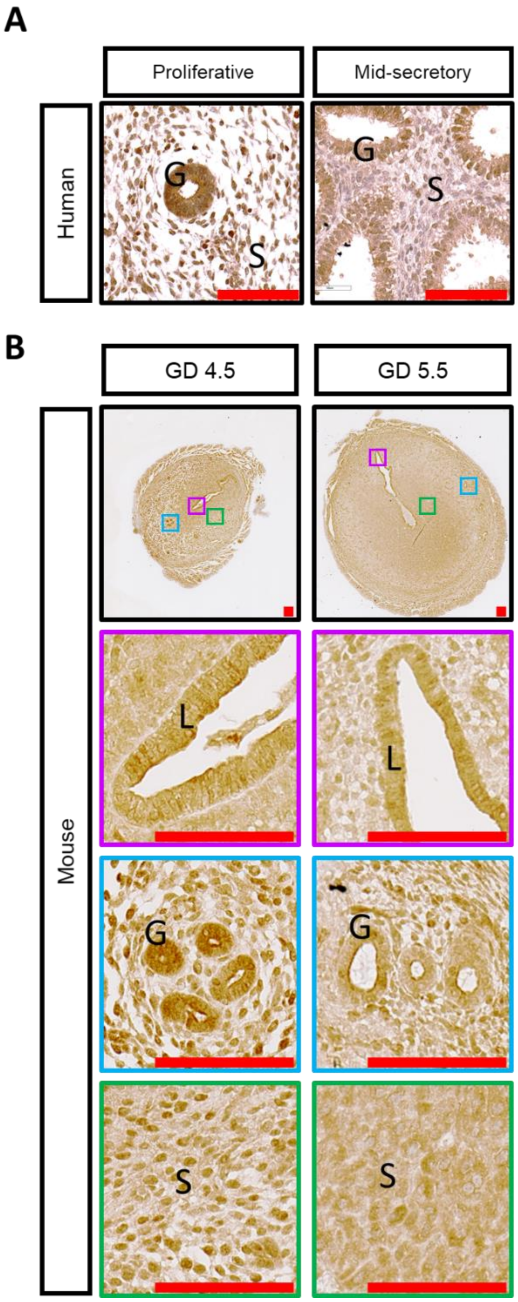

Figure 1. WNK1 is expressed in all compartments of the uterus during the window of implantation in both humans and mice. (A and B) IHC staining of WNK1 in proliferative and mid-secretory phased endometrial tissues from fertile women (A), and during receptive GD 4.5 and post implantation/decidualizing phase GD 5.5 in the uterus of wild-type mice, with the coloured squares indicating positions of enlarged areas (B). G = glandular epithelium, S = stroma and L = luminal epithelium, scale bars = 100 µm.

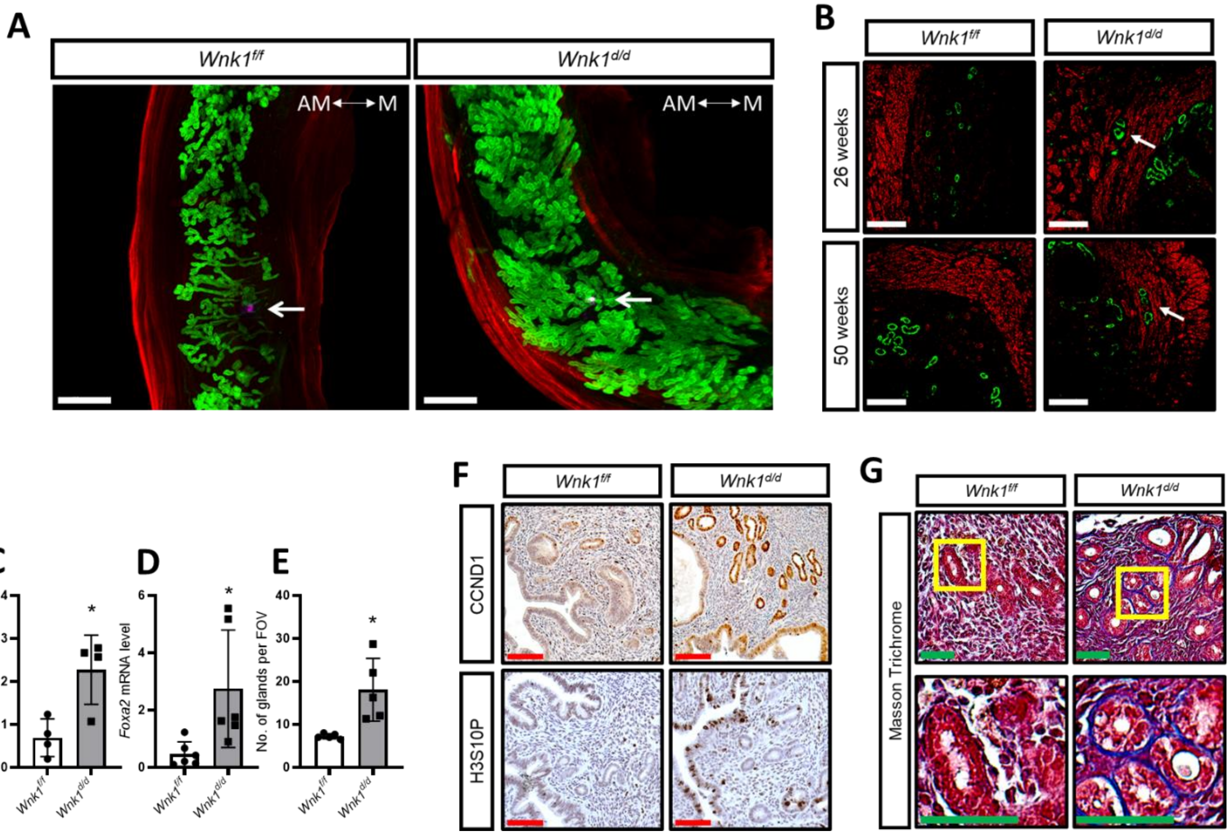

Figure 2. WNK1 ablation altered uterine morphology and microenvironment. (A) 3D reconstruction of *Wnk1*$^{f/f}$ and *Wnk1*$^{d/d}$ uteri on GD 4.5 using tissue clearing and confocal microscopy. The glands, myometrium and embryo were marked by FOXA2 (green), ACTA2 (red) and OCT4 (purple), respectively. Images were captured by tile-scanning and Z-stacking, and reassembled *in silico* using Imaris software. White arrow indicates position of the embryo. Scale bars = 500 µm. The antimesometrial (AM) and mesometrial (M) sides of the tissue are indicated. (B) Immunofluorescence of uterine cross section showing glands (FOXA2, green) and myometrium (ACTA2, red) from *Wnk1*$^{f/f}$ and *Wnk1*$^{d/d}$ uteri. White arrows indicate gland extension into myometrium. Scale bars = 50 µm. (C) Adenomyosis biomarker *Msn* mRNA expression as determined by qRT-PCR (n = 4). (D) Quantification of *Foxa2* mRNA expression as determined by qRT-PCR (n = 6), and (E) Number of glands per cross section for *Wnk1*$^{f/f}$ and *Wnk1*$^{d/d}$ mice (n = 6). (F) Expression of mitotic markers CCND1 and H3S10P in the uterus of 26-week-old *Wnk1*$^{f/f}$ and *Wnk1*$^{d/d}$ mice, scale bars = 100 µm. (G) Masson's trichrome staining of uterine cross section from 26 and 50 week-old *Wnk1*$^{f/f}$ and *Wnk1*$^{d/d}$ mice, scale bars = 100 µm. Yellow boxes indicate region shown at higher magnification in lower panels. All quantitative results shown are mean ± SD, * $p < 0.05$. All *t*-test were 2 tailed, Student's *t*-test (C and E), and Mann-Whitney *U* test (D).

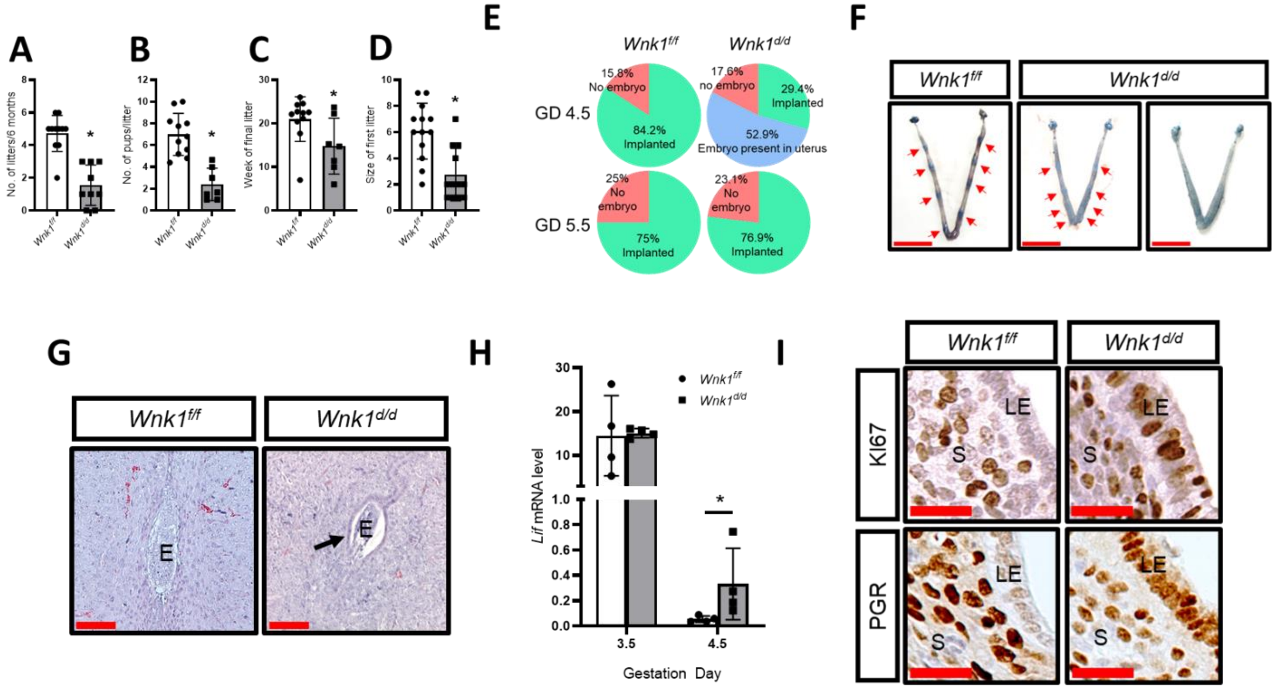

Figure 3. Uterine WNK1 ablation compromised fertility and impaired implantation in mice. (A - D) Results from a 6-month breeding trial, showing (A) average number of litters produced per mouse, (B) average number of pups per litter, (C) time of last delivery from the onset of the breeding trial, and (D) average size of the first litters, n = 11 for *Wnk1*$^{f/f}$ and n = 9 for *Wnk1*$^{d/d}$ mice (A), and n = 11 for *Wnk1*$^{f/f}$ and n = 7 for *Wnk1*$^{d/d}$ (B and C), and n = 13 for *Wnk1*$^{f/f}$ and n = 12 for *Wnk1*$^{d/d}$ (D). Results shown are mean ± SD, * $p < 0.05$. (E) Percentage of mated *Wnk1*$^{f/f}$ and *Wnk1*$^{d/d}$ mice with implantation (green), without implantation (pink), and without implantation but presented embryos in the uterus (blue) on GD 4.5 and GD 5.5, n = 19 and 12 for *Wnk1*$^{f/f}$ mice on GD 4.5 and GD 5.5, respectively; and n = 17 and 13 for *Wnk1*$^{d/d}$ mice on GD 4.5 and GD 5.5, respectively. (F) Gross uterine morphology of *Wnk1*$^{f/f}$ and *Wnk1*$^{d/d}$ mice on GD 4.5, with the implantation sites marked by Evans blue dye, scale bars = 1 cm. Red arrows indicate position of implantation sites. (G) Hematoxylin and eosin staining of uterine cross sections at implantation site on GD 5.5 in *Wnk1*$^{f/f}$ and *Wnk1*$^{d/d}$ mice, arrow indicates presence of uterine epithelium, and E = embryo. Scale bars = 100 µm. (H) Implantation marker *Lif* mRNA expression in the uteri as determined by qRT-PCR on GD 3.5 and PPD 4.5 for *Wnk1*$^{f/f}$ and *Wnk1*$^{d/d}$ mice. Results shown are mean ± SD, * $p < 0.05$, n = 4. (I) Expression of proliferative marker KI67 and implantation marker PGR on GD 4.5 in the stroma and epithelium of *Wnk1*$^{f/f}$ and *Wnk1*$^{d/d}$ mice. LE = luminal epithelium and S = stroma, scale bars = 25 µm. All *t*-test were 2 tailed, Student's *t*-test (B and H), Mann-Whitney *U* test (A, C and D), and Fisher's exact test (E).

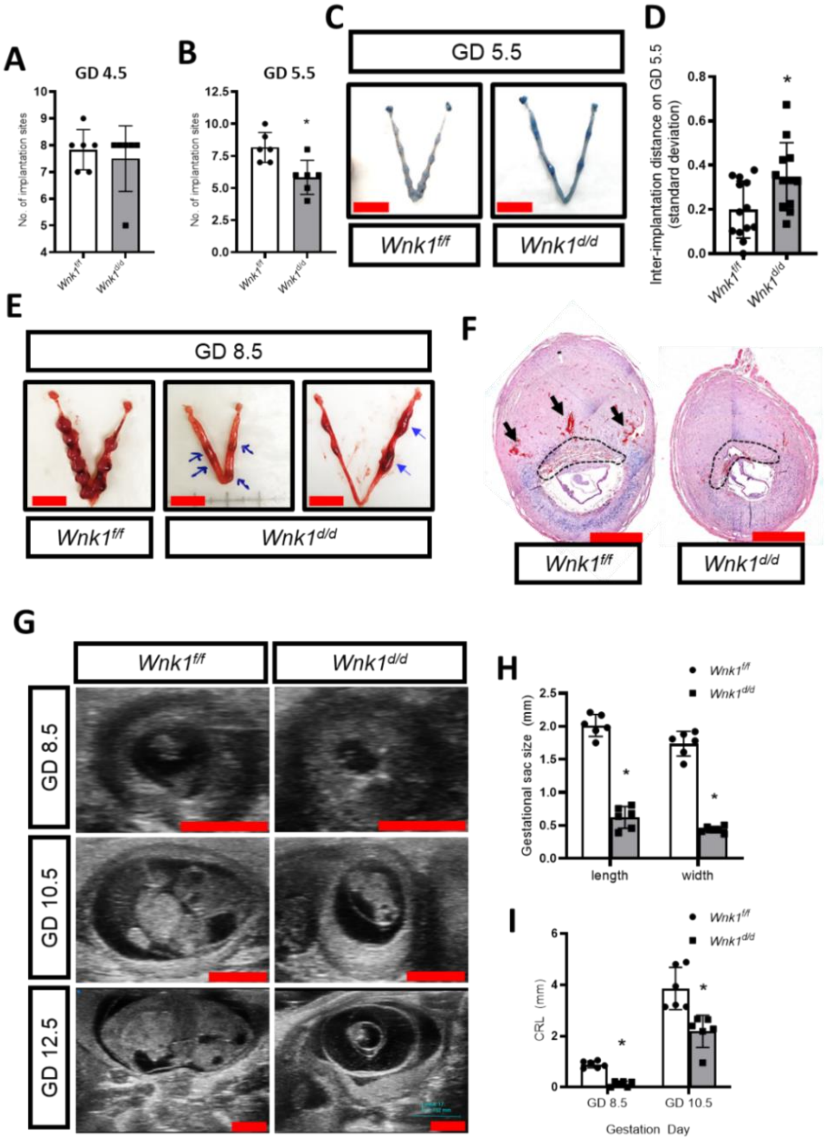

Figure 4. Abnormal embryo development and increased resorption in *Wnk1*$^{d/d}$ mice. (A – B) Number of implantation sites on GD 4.5 (A) and GD 5.5 (B) in *Wnk1*$^{f/f}$ and *Wnk1*$^{d/d}$ mice (n = 6). (C, E) Uterine gross morphology on GD 5.5 (C) and GD 8.5 (E), with implantation sites on GD 5.5 marked by Evans blue dye, and blue arrows indicate resorption and abnormal decidualization on GD 8.5. Scale bars = 1 cm. (D) Comparison of the standard deviation of inter-implantation distance in *Wnk1*$^{f/f}$ and *Wnk1*$^{d/d}$ mice (n= ≥ 12 uterine horns, 7 mice per genotype). (F) Hematoxylin and eosin staining of cross section through the centre of decidual mass on GD 8.5 from *Wnk1*$^{f/f}$ and *Wnk1*$^{d/d}$ mice, with black arrows and dashed line indicating decidual vessels and placental tissues, respectively. Scale bars = 1 mm. (G) Ultrasound scans of uterus and embryo during mid-pregnancy at GD 8.5, 10.5 and 12.5. Scale bars = 2 mm. (H and I) Quantification of gestational sac size by length and width on GD 8.5 (H), and embryo size by crown-rump length (CRL) on GD 8.5 and 10.5, as measured from ultrasound scans (I, n = 6). All quantitative results shown are mean ± SD, * $p < 0.05$. All *t*-test were 2 tailed, Student's *t*-test (B and D), and Mann-Whitney *U* test (A, H and I).

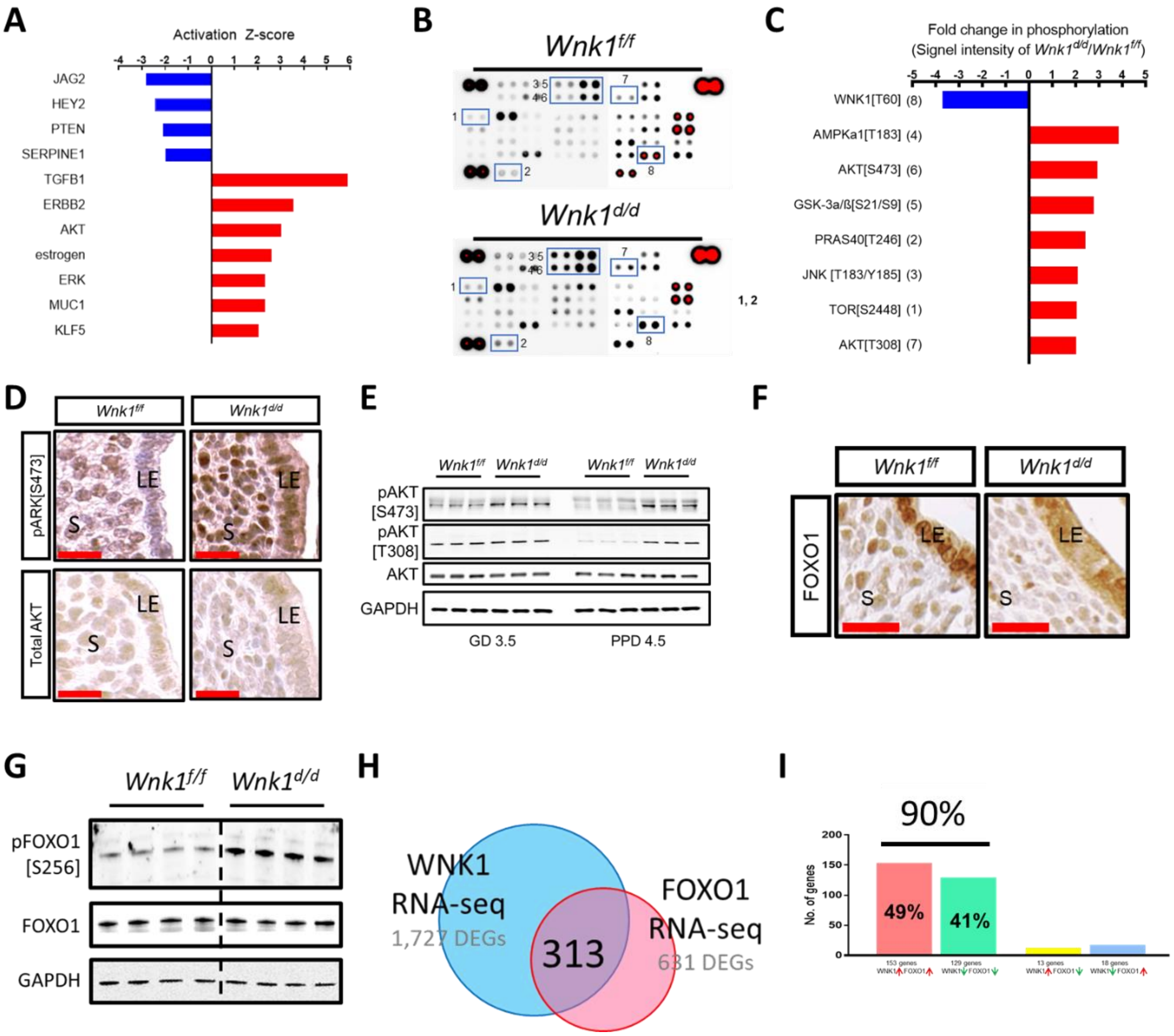

Figure 5. Loss of uterine WNK1 elevated AKT signaling. (A) Activity of upstream regulators as predicted by IPA based on the altered uterine transcriptome of *Wnk1*$^{d/d}$ mice on PPD 4.5. See Table S5 for complete list. (B and C) Kinome phosphorylation status in *Wnk1*$^{d/d}$ and *Wnk1*$^{f/f}$ uteri on PPD 4.5, with selected alterations shown in (C). All kinases with > 1.5 FC in signal intensity as quantified by ImageJ is shown in Fig. S4. Results were acquired using pooled uterine lysate from 6 mice in each group. (D and E) Expression of phosphorylated and total AKT in *Wnk1*$^{f/f}$ and *Wnk1*$^{d/d}$ uteri on GD 4.5 as shown by IHC ((D), LE = luminal epithelium and S = stroma), and on GD 3.5 and PPD 4.5 as shown by Western blotting (E), scale bars = 25 µm. (F) Expression of AKT-regulated implantation marker FOXO1 on GD 4.5 in the stroma and epithelium of *Wnk1*$^{f/f}$ and *Wnk1*$^{d/d}$ mice. LE = luminal epithelium and S = stroma, scale bar = 25 µm. (G) Western blot analysis showing levels of phosphorylated and total FOXO1 in *Wnk1*$^{f/f}$ and *Wnk1*$^{d/d}$ uteri on PPD 4.5. (H) Comparison of DEGs between the uteri of *Wnk1* ablated mice vs. their control littermates (1,727 DEGs; blue) and *Foxo1* ablated mice vs. their control littermates (631 DEGs; pink) identified 313 common genes. (I) Percentage of the 313 genes categorized into commonly upregulated (pink), commonly downregulated (green), or upregulated in one and downregulated in the other (yellow and blue).

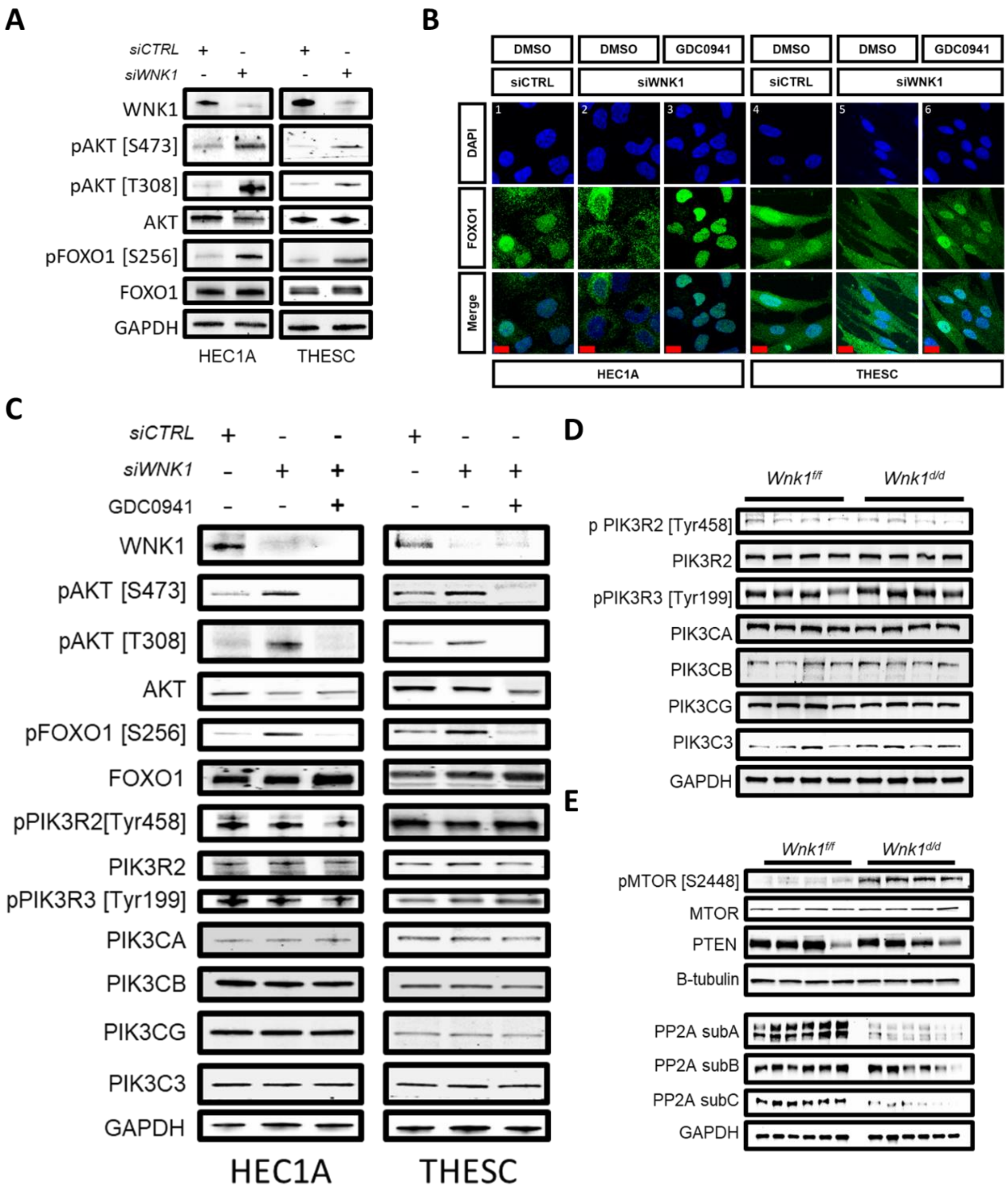

Figure 6. *WNK1* ablation led to FOXO1 nuclear exclusion via AKT phosphorylation which is associated with decreased PP2A phosphatase expression. (A) Western blot showing levels of phosphorylated and total AKT and FOXO1 in HEC1A and THESC cells transfected with 48 nM *siCTRL* or *siWNK1*. (B) Immunofluorescence showing FOXO1 subcellular localization (green), with nuclei presented in DAPI in HEC1A and THESC control cells (1, 4), *siWNK1* transfected cells (2, 5), and GDC0941 treated, *siWNK1* transfected cells (3, 6), scale bars = 20 µm. (C) Expression of FOXO1, AKT and PI3K members in HEC1A and THESC cells transfected with *siCTRL*, *siWNK1*, and treated with AKT inhibitor GDC0941. (D and E) Expression of PI3K proteins (D), and MTOR, PP2A subunits and PTEN (E) in *Wnk1*$^{f/f}$ and *Wnk1*$^{d/d}$ uteri on PPD 4.5.

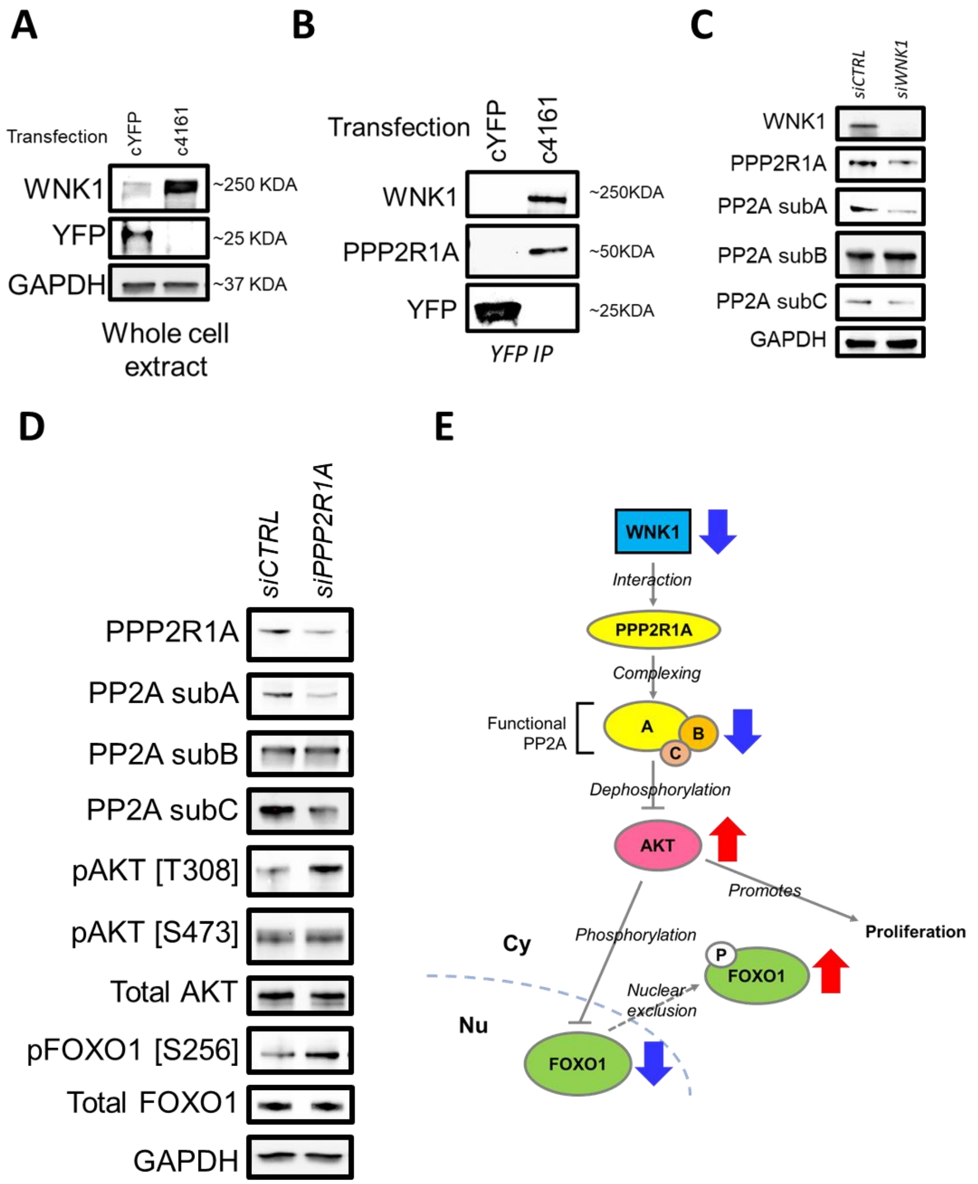

Figure 7. WNK1 regulates AKT signaling through direct interaction with PPP2R1A. (A) WNK1 and YFP expression in HEC1A cells transfected the YFP expressing control plasmid (cYFP) or YFP-tagged WNK1 expression construct (c4161). (B) Co-immunoprecipitation of WNK1 and PPP2R1A with YFP from HEC1A whole cell lysate, as indicated by western blotting. (C) Expression of PPP2R1A and PP2A subunits in HEC1A cells transfected with 24 nM *siCTRL* or *siWNK1* for 72 hours. (D) Expression of PP2A subunits A, B and C, AKT and FOXO1 in HEC1A cells transfected with 72 nM *siCTRL* or siPPP2R1A for 72 hours. (E) Diagram illustrating the WNK1-PPP2A-AKT-FOXO1 signaling axis. WNK1 physically interact with PPP2R1A, the alpha isoform of the scaffold subunit that forms the functional PP2A subunit. PP2A negatively regulates AKT, and AKT negatively regulates FOXO1 by phosphorylation and nuclear exclusion. AKT also promotes epithelial cell proliferation. As indicated by the blue and red arrows, decreased or loss of WNK1 will then lead to decreased PP2A activity, AKT hypersignaling and increased cytoplasmic FOXO1 retention and epithelial proliferation.